J. Fluid Mech. (1999), *vol.* 387, *pp.* 281–320. Printed in the United Kingdom

Evolution and modelling of subgrid scales during rapid straining of turbulence

By SHEWEN LIU[1], JOSEPH KATZ[1,2] AND CHARLES MENEVEAU[1,2]

[1]Department of Mechanical Engineering, The Johns Hopkins University, Baltimore MD 21218, USA

[2]Center for Environmental and Applied Fluid Mechanics, The Johns Hopkins University, Baltimore, MD 21218, USA

(Received 23 June 1997 and in revised form 26 November 1998)

The response, evolution, and modelling of subgrid-scale (SGS) stresses during rapid straining of turbulence is studied experimentally. Nearly isotropic turbulence with low mean velocity and $R_\lambda \sim 290$ is generated in a water tank by means of spinning grids. Rapid straining (axisymmetric expansion) is achieved with two disks pushed towards each other at rates that for a while generate a constant strain rate. Time-resolved, two-dimensional velocity measurements are performed using cinematic PIV. The SGS stress is subdivided to a stress due to the mean distortion, a cross-term (the interaction between the mean and turbulence), and the turbulent SGS stress $\tau_{ij}^{(T)}$. Analysis of the time evolution of $\tau_{ij}^{(T)}$ at various filter scales shows that all scales are more isotropic than the prediction of rapid distortion theory, with increasing isotropy as scales decrease. *A priori* tests show that rapid straining does not affect the high correlation and low square-error exhibited by the similarity model. Analysis of the evolution of total SGS energy dissipation reveals, surprisingly, that the Smagorinsky model with a constant coefficient (determined from isotropic turbulence data) underpredicts the dissipation during rapid straining. While the partial dissipation $-\langle\tau_{ij}^{(T)}\tilde{S}_{ij}\rangle$ (due only to the turbulent part of the stress) is overpredicted by the Smagorinsky model, addition of the cross-terms reverses the trend. The similarity model with a constant coefficient appropriate for isotropic turbulence, on the other hand, overpredicts SGS dissipation. Owing to these opposite trends a linear combination of both models (mixed model) provides better prediction of SGS dissipation during rapid straining. However, the mixed model with coefficients determined from dissipation balance underpredicts the SGS stress.

1. Introduction

Large-eddy simulation (LES) of turbulent flows is based on the filtered Navier–Stokes equations

$$\frac{\partial\tilde{u}_i}{\partial x_i} = 0, \quad \frac{\partial\tilde{u}_i}{\partial t} + \tilde{u}_j\frac{\partial\tilde{u}_i}{\partial x_j} = -\frac{\partial}{\partial x_j}\left(\frac{\tilde{p}}{\rho}\delta_{ij} + \tau_{ij}\right) + \nu\frac{\partial^2\tilde{u}_i}{\partial x_j^2}. \tag{1.1}$$

Here, a tilde represents a filtering operation at some scale Δ, ideally in the inertial range of turbulence. The subgrid-scale (SGS) stress is defined as

$$\tau_{ij} = \widetilde{u_iu_j} - \tilde{u}_i\tilde{u}_j, \tag{1.2}$$

and it must be modelled in terms of the resolved velocity field. Several review articles have already appeared on the subject of LES. Rogallo & Moin (1984) give an account of the traditional status of the subject, while Lesieur & Métais (1996) review more recent developments in SGS modelling. Unlike the Reynolds stress, the SGS stress is a fluctuating variable. From a statistical perspective, several averaged features of the SGS stress are important. For instance, its mean value $\langle \tau_{ij} \rangle$ directly affects transport of mean resolved momentum in non-homogeneous flows, especially if the filter scale is not much smaller than the turbulences integral scale as is often the case. The correlation of the stress with the strain-rate, $-\langle \tau_{ij} \tilde{S}_{ij} \rangle$, the SGS dissipation rate, represents the rate at which resolved energy is 'dissipated' to unresolved scales (Deardorff 1970; Leonard 1974; Piomelli *et al.* 1991). This term is dominant in the turbulent kinetic energy budget at any filter scale in the inertial range. Hence, SGS dissipation is a feature that models must reproduce accurately. We are also interested in the spatial and temporal distribution of the stress in a given realization of the flow, to examine its relation to local physical phenomena and models. Fundamental properties of the SGS stress can be studied by using fully resolved turbulent fields to calculate the real SGS stress according to its definition, and to compare it with model predictions (*a priori* studies). This fully resolved turbulence can be obtained from direct numerical simulation (DNS) data, an approach pioneered by Clark, Ferziger & Reynolds (1979), McMillan & Ferziger (1980), or from experimental data (e.g. Liu, Meneveau & Katz 1994). The latter approach allows investigation of higher-Reynolds-number flows than DNS. Consequently the filter can be significantly varied and maintained away from either end of the inertial range. For example, Liu, Meneveau & Katz (1994, 1995) used PIV to measure a set of instantaneous turbulence velocity fields in the far field of a round jet at a Taylor-scale Reynolds number of $R_\lambda \sim 310$. Cook & Riley (1994) used scalar concentration measurements to study issues related to subgrid modelling in combustion. O'Neil & Meneveau (1997) used hot-wire measurements in the wake of a cylinder to study the spatial distribution of SGS dissipation across the wake.

1.1. *SGS models*

The most traditional and still widely used model for the SGS stress is due to Smagorinsky (1963). The deviatoric part of the stress, $\tau_{ij} - \frac{1}{3}\tau_{kk}\delta_{ij}$, is modelled according to

$$\mathscr{T}_{ij}^{(S)} = -2(c_s \Delta)^2 |\tilde{S}| \tilde{S}_{ij}, \tag{1.3}$$

where Δ is the filter scale and c_S is the Smagorinsky coefficient. While this model has proven to be fairly robust during simulations, it has several drawbacks: among them, the Smagorinsky coefficient, c_S, is flow dependent. Most notably, it should vanish for wall-bounded flows near the wall (Rogallo & Moin 1984), in laminar portions of transitional flows (Piomelli & Zang 1991), and when the filter-scale approaches the Kolmogorov scale (Voke 1996). In shear flows, the coefficient required to yield good predictions of mean flow properties has been found to be smaller than the coefficient appropriate for isotropic turbulence (Rogallo & Moin 1984). These problems have been largely overcome by the dynamic procedure (Germano *et al.* 1991; Lilly 1992; Meneveau, Lund & Cabot 1996) which consists of obtaining the model coefficient from the simulated velocity field itself, without arbitrary adjustments. Another problem that has been observed during *a priori* tests, is that local and instantaneous distributions of real stresses for a given realization of the flow are very different from those obtained using any eddy viscosity models (Clark *et al.* 1977; McMillan & Ferziger 1980; Bardina, Ferziger & Reynolds 1980; Liu *et al.* 1994; Meneveau 1994, etc.). This

discrepancy occurs in part due to a lack of alignment between the stress and strain-rate tensors, a familiar problem in turbulence modelling in the Reynolds-averaged (RANS) context (see e.g. Speziale 1991). This problem reappears in the LES context due to the absence of scale separation between the smallest resolved and largest subgrid flow features, which precludes the small scales from reacting to the large-scale shear quickly enough for the eddy-viscosity closure to be justified. Other variants of the eddy-viscosity SGS model are not exempt from this problem. Included are spectral eddy-viscosity (Kraichnan 1976; Chollet & Lesieur 1981), the structure-function model (Lesieur & Métais 1996), RNG-derived eddy viscosity (Yakhot, Orszag & Yakhot 1989), etc.

While the dynamic procedure interrogates the smallest resolved scales to determine a scalar coefficient for a prescribed base model, the so-called similarity models, originally proposed by Bardina *et al.* (1980) and Bardina (1983), examine the tensorial form of the smallest resolved scales. In the Bardina model, a stress tensor is formed by employing a repeated filtering of the resolved velocity, at the same grid scale Δ. In our previous work (Liu *et al.* 1994, 1995), detailed analysis of velocity fields and energy fluxes between different scales of motion led to the conclusion that an improved model is obtained if the second filtering is performed at a scale 2Δ instead of Δ. This model is written as

$$\mathscr{T}_{ij}^{(L)} = c_L L_{ij}, \quad L_{ij} = \overline{\tilde{u}_i \tilde{u}_j} - \bar{\tilde{u}}_i \bar{\tilde{u}}_j, \tag{1.4}$$

where c_L is the similarity coefficient and the overbar represents filtering at scale 2Δ. L_{ij} is called the resolved stress. This model has provided good local agreement with the real stress distributions (Liu *et al.* 1994, 1995), as quantified by their correlation coefficient (which is about 0.6 instead of 0.1–0.2 for the Smagorinsky model). This model can also provide backscatter, i.e. the flux of kinetic energy from subgrid to resolved scales. It has been studied by Piomelli, Yu & Adrian (1996), who used conditional averaging in channel-flow DNS to examine flow structures associated with particular features of the SGS dissipation. They found that the similarity model yielded structures that closely resemble the real conditional structures, while those obtained with the eddy-viscosity model are considerably different. In another study (O'Neil & Meneveau 1997), conditional averaging of high-Reynolds-number data was employed to examine SGS dissipation in the coherent structures in the wake of cylinder. Again, the similarity model reproduced significantly improved conditional statistics as compared to the eddy-viscosity model. By Taylor-series expansion, the similarity model can be related to a nonlinear model (Liu *et al.* 1994) which has been further explored in Borue & Orszag (1998). Instead of specifying a fixed value for c_L, it can also be obtained using a dynamic procedure (Liu *et al.* 1994, 1995). For consistency a second test filter at scale 4Δ is employed, and the coefficient is computed from the resolved scales. As with the original Bardina model, simulations show that the similarity model must be supplemented with a second term of the Smagorinsky form (mixed model), in order to generate sufficient dissipation during a simulation. The experimental data in the round jet (Liu *et al.* 1994, 1995) showed that the mixed model combines the advantages of both models: the Smagorinsky part guarantees that there is some SGS dissipation; while the dominant similarity part achieves a more realistic description of the SGS stress field, including both forward- and backscatter of energy. For additional *a priori* tests in equilibrium turbulent flows that support the mixed model, see Vreman, Guerts & Kuerten (1994), Salvetti & Banerjee (1995), Piomelli *et al.* (1996), and Ansari *et al.* (1998). Moreover, mixed models in various forms (dynamic and non-dynamic) have recently been applied in a growing number

of simulations, including recirculating flows (Zang, Street & Koseff 1993), boundary layers (Wu & Squires 1997; Horiuti 1997), mixing layers (Vreman, Guerts & Kuerten, 1997) and jets (Kang, Ansari & Akhavan 1998), with promising results.

1.2. *Rapid distortion*

Most previous *a priori* studies of SGS models have focused on equilibrium turbulence, i.e. flows in which turbulence time scales are comparable to changes in the mean flow. Canonical flows such as the round jet, plane wake, fully developed channel flow, etc. fall into this category. The goal of the present study is to examine the response of subgrid scales, and their modelling with eddy-viscosity and similarity models, during strong perturbation from an equilibrium state. Such modification can be achieved for example by rapidly straining initially isotropic turbulence. A substantial amount of work has been devoted to predicting the response of initially isotropic turbulence to rapid straining, from the point of view of RANS variables. When the magnitude of the applied straining is very large compared to the characteristic inverse turbulence time scale, the short-time evolution of Reynolds stresses may be predicted using rapid distortion theory (RDT) (Batchelor & Proudman 1954; Townsend 1976; Crow 1968 and more recently Savill 1987; Kida & Hunt 1989; and Hunt & Carruthers 1990). Currently, the RDT-calculated response of Reynolds-averaged quantities to rapid distortions is employed for calibrating RANS models (e.g. Speziale 1991; Kassinos 1994).

Rapid straining has been studied in the past by performing measurements at several downstream distances along especially designed wind-tunnel contractions (e.g. Tucker & Reynolds 1968; Gence & Mathieu 1979). Predictions from RDT have been confirmed, for short times. For weak axisymmetric expansion, when RDT is not applicable, Choi (1983) and Lee (1985) surprisingly obtained larger anisotropy for the Reynolds stress than was predicted by RDT. This feature will be discussed and compared to the present data later. Turbulence subjected to sudden shear (strain plus rotation) has also been widely studied (Champagne, Harris & Corrsin 1970; Sreenivasan 1985; Tavoularis & Corrsin 1981; and Tavoularis & Karnik 1989). In addition, some research has focused on the impact of straining on coherent structures (e.g. Devenport & Simpson 1990).

While these extensive studies have focused on Reynolds-stress evolution and spectra, not much is known about the response of SGS stresses, SGS dissipation and models to rapid distortion. McMillan *et al.* (1980) used DNS of isotropic turbulence at $R_\lambda \sim 40$ to study the response of SGS models to plane strain, and several observations were made on model coefficients and correlations. We will return to their results later on. Smith & Yakhot (1993) point out the possibility that at short times the Smagorinsky SGS model would respond too quickly to applied shear (the notion that the eddy-viscosity approximation fails at short times for Reynolds stresses dates further back, see e.g. Crow 1968). LES of rapidly distorted turbulence is complicated by the appearance of a new characteristic length scale $L^* = \epsilon^{1/2} S^{*-3/2}$ (ϵ is the dissipation rate and S^* is the mean strain magnitude). One should expect the subgrid scales to respond differently depending on Δ/L^*. In the limit $\Delta/L^* \to 0$, the time scale associated with the subgrid eddies is short enough for their response to be 'fast'. Consequently, one would expect that the applied distortion does not directly affect the subgrid range. Indeed, Saddoughi (1993) studied energy spectra in an approximately planar expansion and found that spectra show isotropy of small scales for wavenumbers above $k \sim 3S^{*3/2}/\epsilon^{1/2}$, and anisotropic behaviour at the larger scales. If $\Delta/L^* \gg 1$ the subgrid turbulence is 'slow' compared to the applied distortion, and its evolution

should be close to RDT predictions. An interesting regime is the transition between these limiting cases, when $\Delta/L^* \sim O(1)$. In a recent paper, Kevlahan & Hunt (1997) consider RDT with planar strains and keep the next terms in the asymptotic expansion. Besides finding important dependences upon the detailed structure of the initial condition, they confirm that the RDT prediction is valid only until a scale-dependent time, which becomes short at small scales.

The present study focuses on the response of SGS variables to rapid straining. In particular, the main objective is to examine the response of the real SGS stress and dissipation, and of the similarity and eddy-viscosity models, to axisymmetric straining. The results are compared with those of equilibrium isotropic turbulence. The experiment entails the sudden generation of an irrotational distortion, consisting of a linear mean flow with $U_i = A^*_{ij}(x_j - x^0_j)$, where $A^*_{ij} = A^*_{ji} = S^*_{ij}$ is the spatially uniform strain-rate tensor. For an axisymmetric expansion, $S^*_{11} = -S^*$, $S^*_{22} = S^*_{33} = S^*/2$, and $S^*_{ij} = 0$ if $i \neq j$. The turbulence and straining are generated in a facility in which the mean convection velocity is low. The experimental setup, instrumentation, and procedures are described in § 2. Section 3 is devoted to a detailed characterization of the initial turbulence and of the applied straining. In § 4, RDT is used to predict the evolution of the mean SGS stress, and the results are compared with the measurements at different filter scales. In § 5, the time evolution of individual flow structures that are visible in band-pass filtered velocity fields at different scales is followed. Implications for local and averaged features of the SGS stress, as well as for the similarity model, are described. As argued before, SGS dissipation is an important feature for LES. Thus, in § 6, we study the evolution of real and modelled SGS dissipation and use the results to obtain appropriate values of the coefficients. Particular attention is paid to the mixed model. The conclusions of the study are presented in § 7. The main findings are as follows. (*a*) During rapid distortion small scales remain more isotropic, but become proportionally more energetic, than the large scales. Deviations from the RDT predictions are observed at all scales. (*b*) When the applied straining is strong, and when spatial filtering is performed in directions where the mean flow is inhomogeneous, the mean flow has a very strong, direct effect on the SGS stress and dissipation rate. (*c*) This effect leads to trends with straining and scale that are better predicted with a mixed model than with eddy-viscosity or similarity models alone. (*d*) Nevertheless, the time evolution of the mean SGS stress is not well reproduced by any of the models considered and may imply the need for time-dependence of the coefficients, possibly to be determined from the dynamic model.

2. Experimental setup

2.1. *Facility*

There are three main requirements for the experimental facility. The first is the generation of isotropic turbulence with turbulence Reynolds number as high as possible in a moderately sized facility. The second requirement is to apply uniform and rapid straining on the turbulence. The straining should be maintained constant for a duration sufficient that the turbulence has enough time to respond and evolve. Thirdly, for convenience and for the capability to follow the same structures in time, it is also advantageous to operate in a facility with relatively low mean velocity.

Several approaches to generate steady isotropic turbulence with low mean velocity have been used. Hopfinger & Toly (1976) used a single oscillating grid to generate stationary isotropic turbulence, but it was not homogeneous since the turbulence

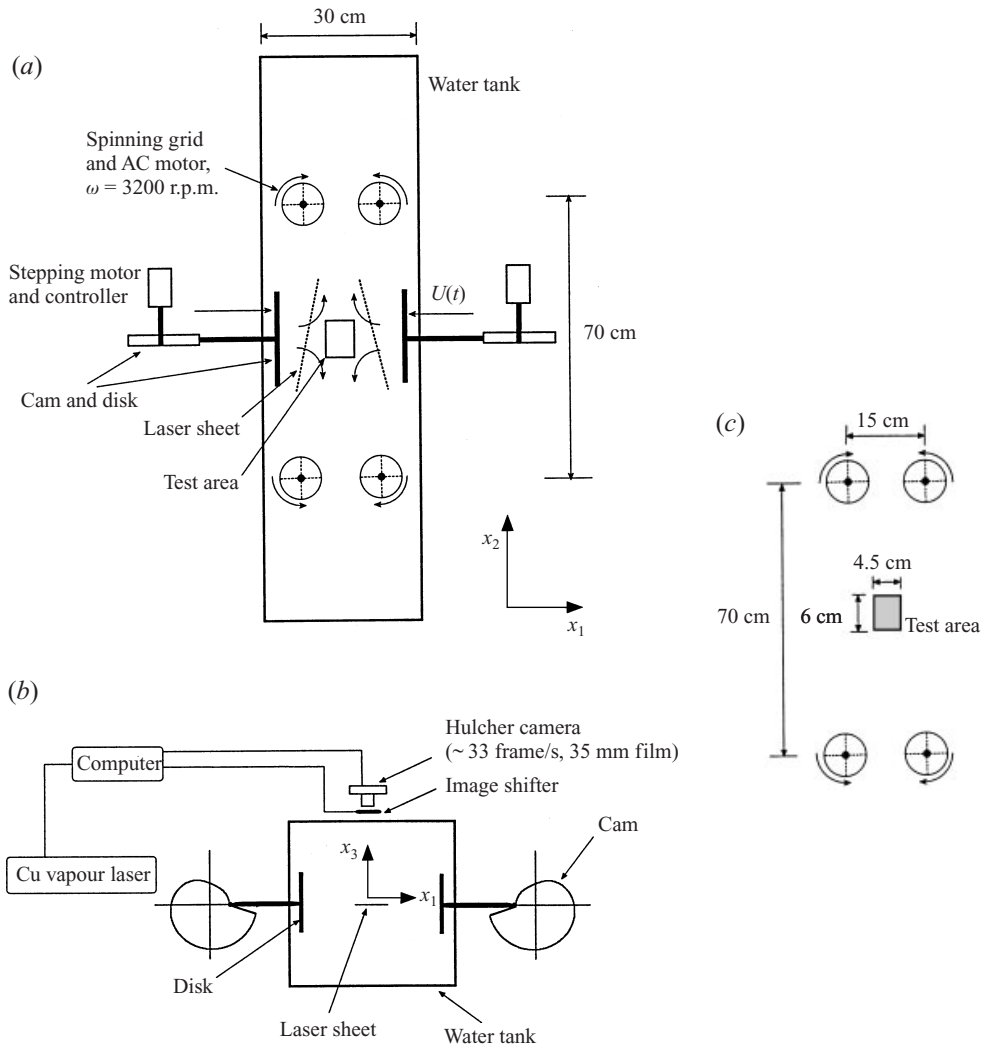

FIGURE 1. Schematics of experimental setup: (*a*) top view, (*b*) side view, (*c*) location of rotating grids for generation of turbulence.

intensity quickly decayed with the distance from the grid. Recently, Srdic, Fernando & Montenegro (1995) used two symmetrically located oscillating grids to produce nearly homogenous turbulence between them. However, the turbulence microscale Reynolds number R_λ achieved in this experiment was low. To generate isotropic turbulence with considerably higher Reynolds number, a different approach is developed and described below.

A schematic description of the experimental facility is shown in figure 1(*a*, *b*). It consists of a 3 m long, 30 cm by 30 cm cross-section, transparent water tank, and two separate mechanical systems. The first generates the turbulent flow, and the second produces the rapid straining. Turbulence is generated by four high-speed rotating grids located symmetrically around the centre of the water tank (see figure 1*c* for more detail). They are driven by four AC motors operating at 3200 rpm. Each of these consists of two 10 cm high and 8.8 cm wide perpendicular grids made of

1 mm diameter wires arranged in a mesh of size M=5 mm (solidity $\sigma = 0.36$). They are supported in the centre by 1.25 cm diameter rods and bounded on the top and bottom by aluminium disks. The purpose of these disks is to substantially reduce the organized axial inflow at the ends and radial outflow through the perimeter. The mean velocity over the measurement region at the centre of the tank is about 0.04 m s^{-1}, low enough for our purpose. By further adjustments of the rotor locations, the mean velocity could be further reduced, but this was not deemed necessary. As will be shown in § 3, the high tip speed of the grid, 14.7 m s^{-1}, creates a high turbulence level, $u_1' \sim 6$ cm s^{-1}, $u_2' \sim 5$ cm s^{-1} and relatively high Reynolds number, $R_\lambda \sim 290$, at the centre of the tank. Furthermore, turbulence spectra (see § 3) are measured to demonstrate that the turbulence generated by this method is locally isotropic in the central measurement region.

The uniform rapid straining is generated by two 15 cm diameter round plates facing each other across the central portion of the tank. Each is attached to a rod actuated by a cam (see figure 1) to produce a stagnation-point-type flow. To precisely control the speed of the plates, the cams are driven by two 8 N-m precision stepping motors with 1000 steps per cycle. In order to produce time-independent straining, the distance between the plate and the stagnation point should be of the form

$$\Delta x(t) = \Delta x(t_0)\exp[-S^*(t - t_0)], \tag{2.1}$$

where $\Delta x(t_0)$ is the initial distance and S^* is the strain rate. Consequently the speed of the plates is

$$U(t) = S^*\Delta x(t). \tag{2.2}$$

The shape of the cams is designed to produce the desired displacement $\Delta x(t)$. Figure 2(a) shows the desired velocity $U(t)$ based on which the cams were designed. A start-up phase is required to accelerate the plate from zero to the maximum speed. It is followed by a deceleration phase during which the distance between plates and the stagnation point should follow (2.1) to produce constant straining. The position of the plates was measured using a movie camera (see § 2.2) during the deceleration phase, and is shown as function of time in figure 2(b). As required for constant straining, $\Delta x(t)$ is well fitted by an exponential curve. The implied rate of strain, $S^* = 8.1$ (s^{-1}), will be shown to be very close to strain rates measured directly from the flow field (see § 3.2). Thus, when both cams are rotated symmetrically at the same time, uniform axisymmetric straining of constant magnitude S^* is generated in most of the region between both plates except for boundary layers developing on them. As verified in § 3, this procedure generates nearly constant axisymmetric expansion of the flow.

2.2. *Instrumentation*

Particle image velocimetry (PIV) is used to measure the velocity field and its time evolution. The measurements are performed on a horizontal plane containing the axis of the plate and the stagnation point during straining. The sample area is a 4.5 × 6 cm^2 (see figure 1). The facility is seeded with 20 μm diameter and neutrally buoyant spherical fluorescent particles (the particle specific gravity is around 0.95–1.05). The light sheet is generated by a 45 W copper vapour laser with a wavelength of 511 nm (the 578 nm is filtered), whose beam is reduced from 5.4 cm to about 1 mm and then expanded to a thin sheet. To record the time evolution of the flow, successive images are recorded on 35 mm Kodak TMAX 3200 film using a Hulcher movie camera equipped with a 105 mm lens and extension tubes, at 33 frame s^{-1}. The magnification is around 0.55. Double-exposure images are recorded. To eliminate the problem of

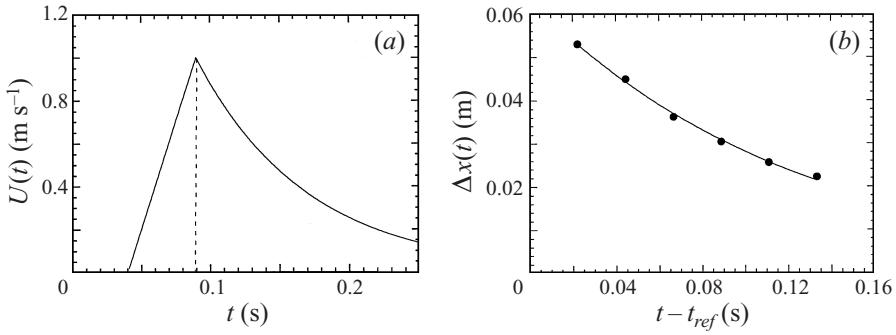

FIGURE 2. (*a*) Desired velocity of plates as a function of time. (*b*) Circles: measured distance between the disk and the centre of the test area during the constant straining phase. Solid line: exponential fit of the form $\Delta x(t) = X^* \exp[-S^*(t - t_{\rm ref}) + t^*]$. The fitted parameters are $t^* = 0.17$ s and $X^* = 0.26$ m (an arbitrary time origin and initial distance), and $S^* = 8.11\,{\rm s}^{-1}$, which corresponds to the strain rate in the flow.

directional ambiguity, an electro-optical image shifting technique is used (Bertuccioli, Gopalan & Katz 1996). The basic idea of this technique is to superimpose a known displacement on the real movement of the second particle trace on the film. The process involves rotating the polarization of light arriving at the camera using a ferroelectric liquid crystal (FLC) and shifting the second image by a calcite crystal. More details of this technique are described in Bertuccioli *et al.* (1996). The laser, movie camera, image shifting device and the cams are synchronized by a PC.

During each run, with the turbulence generators running, the Hulcher camera starts recording two images of the turbulent flow field before straining. Then, the cams are activated, the round disks are accelerated to $U(t_0) = \Delta x(t_0)S^*$, and then decelerated exponentially (as in (2.1)) imposing constant and uniform rapid straining on the flow. The Hulcher camera continues to record pictures during the straining phase. Each data set consists of 10 images and the time delay between 2 images is 0.03 s. Results of 10 such experiments are used during data analysis. The negatives are scanned using a Nikon 3500, 35 mm slide scanner. Each image is converted to a 2048×3072 pixels array which is then filtered and enhanced (Dong, Chu & Katz 1992; Roth, Hart & Katz 1995). The autocorrelation method is used to compute the velocity. The interrogation window is 64×64 pixels, which corresponds to a 1.4×1.4 mm window in the actual flow. The velocity is evaluated every 32 pixels (50% overlap) providing a grid spacing of $d = 0.68$ mm. Sub-pixel accuracy (about 0.2–0.4 pixels) is achieved by interpolating between the discretely computed values of the auto-correlation function (Dong *et al.* 1992; Roth *et al.* 1995). The relative error of the velocity is about 1% which means that the uncertainty in rate of strain determined from the velocity is of the order of 10% (Ganapathy & Katz 1995). To quantify the isotropy of the initial turbulence, we also measure the velocity field on a vertical plane perpendicular to the original test area.

3. Flow characterization

The basic flow characterization is described in this section. Figure 3(*a*) shows a sample vector map of the turbulent flow field before the straining starts and figure 3(*b*) is the flow at a certain time during the rapid straining. The superposition of turbulence and strong stagnation-point flow is clearly evident.

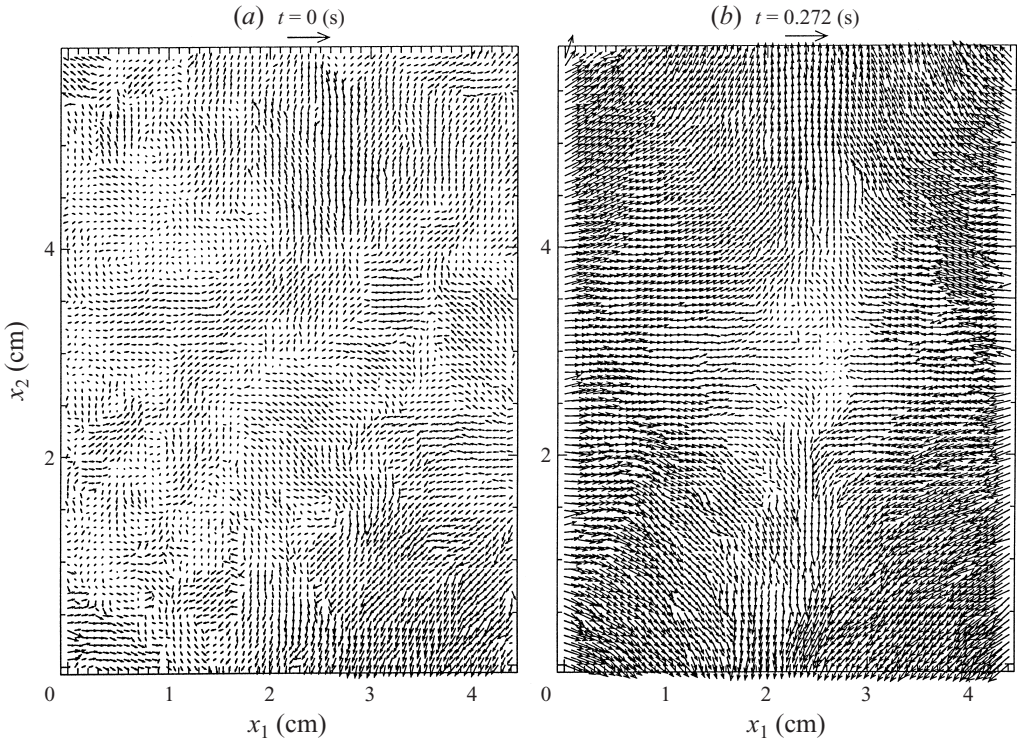

FIGURE 3. Vector maps of velocity field (*a*) before straining, at $t = 0$ s, (*b*) during straining at $t = 0.272$ s. The reference vector at the top has magnitude $0.5\,\mathrm{m\,s^{-1}}$. The mean velocity over the image has been subtracted.

3.1. *Turbulence before straining*

3.1.1. *Basic scales*

The mean velocity prior to straining computed over 20 images is $\langle u_1 \rangle \approx 0.043\,\mathrm{m\,s^{-1}}$ and $\langle u_2 \rangle \approx 0.013$. These values are significantly smaller than velocity magnitudes prevalent during rapid straining. The r.m.s. values are $u_1' \approx 0.06\,\mathrm{m\,s^{-1}}$ and $u_2' \approx 0.051\,\mathrm{m\,s^{-1}}$, indicating a 15% anisotropy of the large-scale turbulence. To quantify anisotropy at scales smaller than or equal to the image size, the mean velocity of each image is subtracted before averaging the variance. The resulting r.m.s. values are $u_1'' \approx 0.038\ \mathrm{m\,s^{-1}}$ and $u_2'' \approx 0.04\,\mathrm{m\,s^{-1}}$, an indication that turbulence is nearly isotropic at scales smaller than the image size. Estimates of the energy dissipation rate and the Kolmogorov scale from the r.m.s. velocity require knowledge of the integral scale ℓ, which we cannot measure from the present data set. Therefore, we obtain the dissipation rate by matching the measured energy spectrum with the prediction of the Kolmogorov spectrum. This procedure is discussed below in detail.

The radial two-dimensional spectrum of both components is obtained from the PIV data, as described in Liu *et al.* (1994). It involves subtracting the mean velocity over the image, windowing the data (using a Welch window), applying FFT, and averaging the modulus over annuli of radius k. For statistical convergence, the spectra are averaged over 20 images. The results are shown in figure 4 (left scale). The insert shows the radial spectra premultiplied with $k^{5/3}$. As a reference, a straight line with a Kolmogorov slope of $-\frac{5}{3}$ is also plotted. This plot shows that the slope of the spectrum

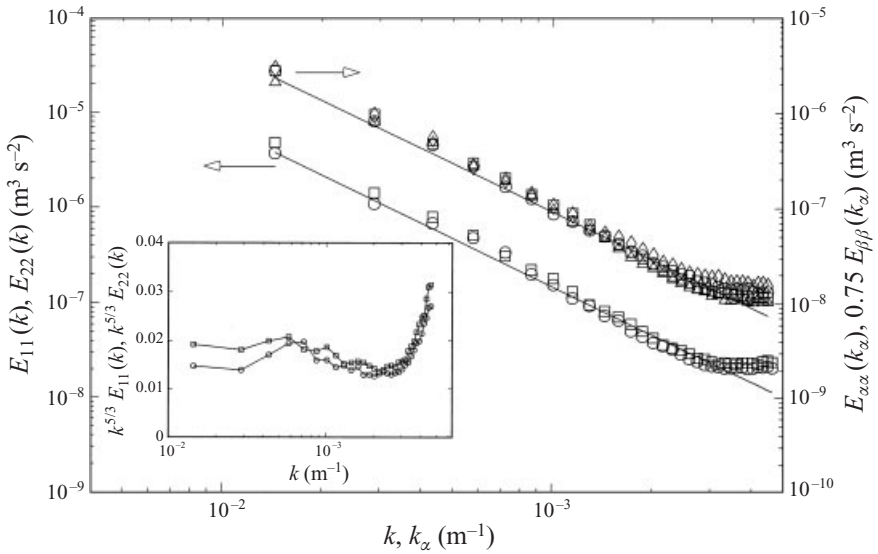

FIGURE 4. Kinetic energy spectra of turbulence before straining. Left scale: two-dimensional radial spectra: $E_{11}(k)$ (open circles), $E_{22}(k)$ (open squares). Right scale: one-dimensional spectra. Circles: $E_{11}(k_1)$, squares: $\frac{3}{4}E_{22}(k_1)$, triangles: $\frac{3}{4}E_{11}(k_2)$, rhombs: $E_{22}(k_2)$. Solid lines: Kolmogorov spectra with $C_K = 1.6$ and $\epsilon_0 = 0.0023\,\mathrm{m^2\,s^{-3}}$. Inset: premultiplied radial spectra.

of both velocity components is near $-\frac{5}{3}$ in most of the resolved range except at the smallest scales where some deviation occurs due to measurement uncertainty (for a more detailed discussion of this issue, see Liu *et al.* 1994). To estimate the energy dissipation, we can match the universal Kolmogorov spectrum,

$$E_{\alpha\alpha}(k) = 0.535 c_k \epsilon^{2/3} k^{-5/3} \text{ (no summation over } \alpha), \tag{3.1}$$

with our experimental data. The factor 0.535 in (3.1) is the coefficient appropriate for a two-dimensional spectrum (Liu *et al.* 1994). When the standard value for the universal Kolmogorov constant, $c_k = 1.6$, is used, $\epsilon_0 \approx 2.3 \times 10^{-3}\,\mathrm{m^2\,s^{-3}}$ for ϵ in (3.1) yields good agreement with the data. The integral length scale estimated using $\epsilon_0 \sim u_1'/\ell$, with $u_1' \approx 0.06\,\mathrm{m\,s^{-1}}$ as velocity scale, is $\ell \approx 9.3\,\mathrm{cm}$. The Kolmogorov scale, calculated from $\eta = (\nu^3/\epsilon_0)^{1/4}$, is 0.14 mm, and the Taylor microscale, λ, is $\lambda = u_1'(15\nu/\epsilon_0)^{1/2} \approx 4.8\,\mathrm{mm}$. It follows that the turbulence microscale Reynolds number is $R_\lambda \approx 290$. This value is substantially higher than that of the DNS data previously used to study rapid distortion of turbulence (Lee 1989; McMillan & Ferziger 1980).

3.1.2. *Isotropy and homogeneity*

To further quantify the level of isotropy of the turbulence in the test region prior to straining, one-dimensional spectra in different directions are computed. The mean velocity along each line is subtracted, and a one-dimensional Welch window is used. Spectra are averaged over all the 20 data sets corresponding to the initial undisturbed state. Both longitudinal and transverse spectra are computed. In the inertial range, the transverse and longitudinal spectra are related by (Monin & Yaglom 1971)

$$E_{22}(k_1) = \tfrac{4}{3}E_{11}(k_1). \tag{3.2}$$

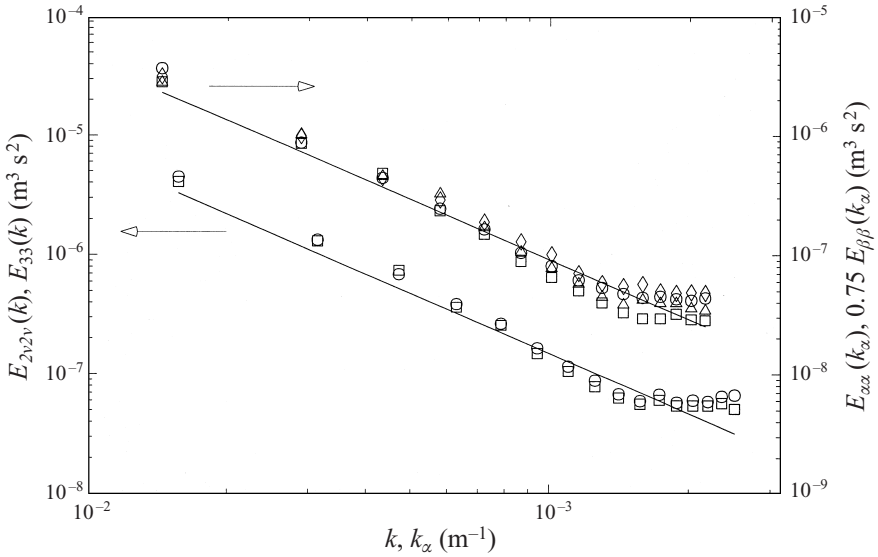

FIGURE 5. Kinetic energy spectra of turbulence before straining in the (x_2, x_3)-plane. Left scale: two-dimensional radial spectra: $E_{2v2v}(k)$ (open circles), $E_{33}(k)$ (open squares). Right scale: one-dimensional spectra. Circles: $E_{22v}(k_2)$, squares: $\frac{3}{4}E_{33}(k_2)$, triangles: $\frac{3}{4}E_{22v}(k_3)$, rhombs: $E_{33}(k_3)$. Solid lines: Kolmogorov spectra with $C_K = 1.6$ and $\epsilon_0 = 0.0023\,\mathrm{m^2\,s^{-3}}$.

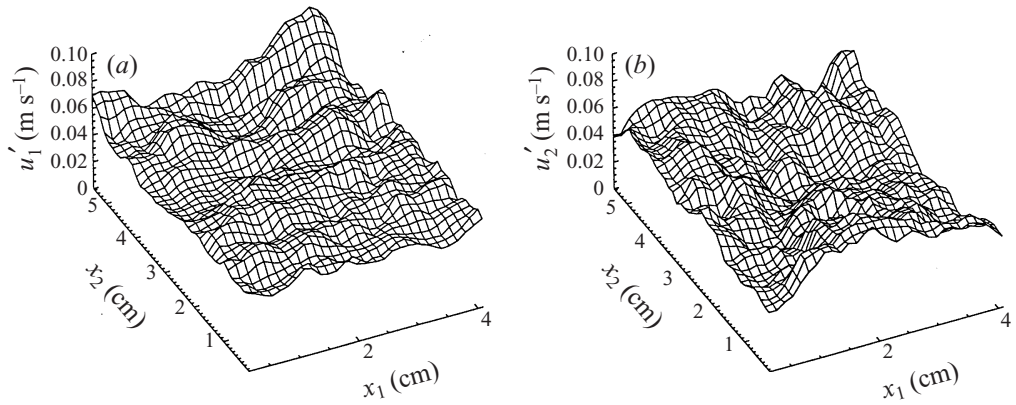

FIGURE 6. Velocity root-mean-square values computed at each point of the vector maps over 20 realizations: (*a*) u_1', (*b*) u_2'. Results are not statistically converged.

Figure 4 (right scale) shows $E_{11}(k_1)$, $E_{22}(k_2)$, $\frac{3}{4}E_{11}(k_2)$, and $\frac{3}{4}E_{22}(k_1)$, as well as the Kolmogorov longitudinal spectrum

$$E_{11}(k_1) = c_k \tfrac{18}{55}\epsilon_0^{2/3}k_1^{-5/3} \tag{3.3}$$

with $c_k = 1.6$ and $\epsilon_0 = 0.0023\,\mathrm{m^2\,s^{-3}}$. Fairly good agreement exists among the various curves, although some discrepancies are observed at large wavenumbers.

To document flow properties in the x_3-direction, we also measure the velocity field in the vertical plane (perpendicular to the plane which is used for most of the data analysis). This plane provides the velocity components in the x_2- and x_3-directions, u_{2v} (the subscript v represents the component in the x_2-direction but in the vertical

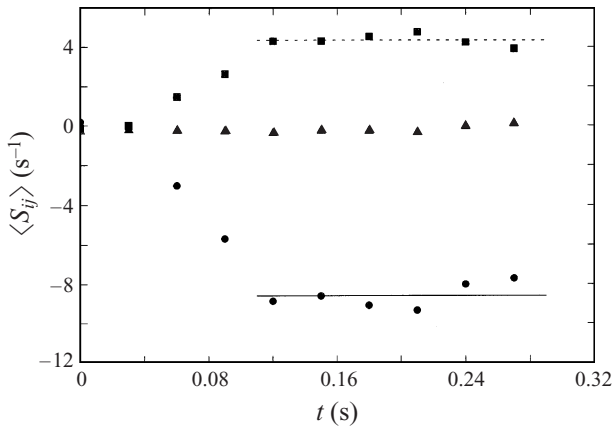

FIGURE 7. Mean rate-of-strain components as function of time. Circles: $\langle S_{11} \rangle$, squares: $\langle S_{22} \rangle$, triangles: $\langle S_{12} \rangle$. Solid lines indicate the mean values during the constant straining stage.

plane) and u_3. Seven images are used. To reduce the processing time, these images are digitized into 1000×1500 pixels, half of the resolution used in the horizontal planes. Thus, each image is converted to 48×32 vectors. The r.m.s. values of the velocity in the vertical plane are $u'_{2v} \approx 0.058\,\mathrm{m\,s^{-1}}$ and $u'_3 \approx 0.051\,\mathrm{m\,s^{-1}}$. Figure 5 (left scale) shows the radial spectra for the vertical plane compared to the Kolmogorov spectrum using $c_k = 1.6$ and $\epsilon_0 = 0.0023\,\mathrm{m^2\,s^{-3}}$. One-dimensional spectra are also shown in figure 5 (right scale). Taken together with the results of figure 4, we conclude that the turbulence is near a locally isotropic state.

The spatial inhomogeneity of turbulence is quantified by calculating the spatial distribution of r.m.s. velocity using ensemble averaging over the 20 data sets. The results are shown in figure 6. They display considerable fluctuations, which are probably caused by the insufficient statistical convergence, a result of using only 20 independent samples. While there are noticeable humps in the distribution, they occur over length scales that are smaller than one would expect for variations in the mean flow. Also, the humps oscillate around a mean value that does not appear to have an obvious trend of spatial variation across the region. We conclude that the flow is sufficiently homogeneous to allow us to evaluate averages over the sample area, as well as over realizations.

3.2. *Applied straining*

In order to verify that the mean flow generated by the disks is an axisymmetric, time-independent straining, the velocity gradients are calculated from the data at the 10 times, using centre finite differencing. The rate-of-strain tensor is obtained according to its definition

$$S_{ij} = \frac{1}{2}\left(\frac{\partial u_i}{\partial x_j} + \frac{\partial u_j}{\partial x_i}\right). \tag{3.4}$$

Figure 7 shows the mean rate of strain (averaged in space and over 10 realizations) as a function of time. For the first two data points, at $t \leqslant 0.03\,\mathrm{s}$, the straining is essentially zero. Thus, data generated during this stage of the experiment represents undisturbed turbulence. The next two points correspond to the acceleration stage. Once the disks start decelerating after $t = 0.12\,\mathrm{s}$, the rate of strain remains nearly constant. At the developed stage ($t \geqslant 0.12\,\mathrm{s}$), the compressive rate of strain $\langle S_{11} \rangle \approx -8.6\,1\,\mathrm{s^{-1}}$ is about

twice the expanding strain $\langle S_{22}\rangle \approx -4.35\ \mathrm{l\,s^{-1}}$ (in magnitude). This ratio is expected for an axisymmetric expansion, for which the strain-rate tensor is given by

$$\langle S_{ij}\rangle = |\langle S_{11}\rangle| \begin{pmatrix} -1 & 0 & 0 \\ 0 & \frac{1}{2} & 0 \\ 0 & 0 & \frac{1}{2} \end{pmatrix}. \tag{3.5}$$

Later on, it will be of interest to separate the turbulence from the applied straining. The latter, linear velocity field is given by

$$U_1(x_1, x_2) = \langle S_{11}\rangle (x_1 - x_1^0), \quad U_2(x_1, x_2) = \langle S_{22}\rangle (x_2 - x_2^0), \tag{3.6}$$

where $\boldsymbol{x}^0$ is the coordinate of the stagnation point. To compare the applied strain-rate magnitude to the turbulence, we evaluate the non-dimensional strain number $S' = S^* k_0/\epsilon_0$, where $S^* = |\langle S_{11}\rangle|$ for the constant straining phase and k_0 is the turbulent kinetic energy prior to straining. The turbulence turnover time is $k_0/\epsilon_0 \approx 2.0\,\mathrm{s}$, while the characteristic time scale of the applied straining is $1/S^* \approx 0.12\,\mathrm{s}$. Their ratio, $S' \sim 17$, is quite large, making the applied straining 'rapid' compared to the large scales of turbulence.

4. Subgrid stress during rapid straining

4.1. *Definitions*

The filtered velocity field at time t is defined in terms of the measured two-dimensional data as

$$\tilde{u}_i(x_1, x_2; t) = \int\int u_i(x_1', x_2'; t) F_\Delta(x_1 - x_1', x_2 - x_2')\mathrm{d}x_1'\mathrm{d}x_2' \quad (i = 1, 2), \tag{4.1}$$

where $F_\Delta(x_1, x_2)$ is a spatial low-pass filter with characteristic width Δ. In this study, a top-hat filter is used. It is defined as $F_\Delta(x_1, x_2) = B$ for $|x_1| < \Delta/2$ and $|x_2| < \Delta/2$, and zero otherwise. The coefficient B is a normalization factor which ensures that the integral of $F_\Delta(x_1, x_2)$ equals unity (in the discrete sense). Similarly, the SGS stress, τ_{ij}, is computed from

$$\tau_{ij}(x_1, x_2; t) = \int\int u_i(x_1', x_2'; t) u_j(x_1', x_2'; t) F_\Delta(x_1 - x_1', x_2 - x_2')\mathrm{d}x_1'\mathrm{d}x_2' - \tilde{u}_i(x_1, x_2; t)\tilde{u}_j(x_1, x_2; t) \quad (i, j = 1, 2). \tag{4.2}$$

The resolved velocity-gradient tensor

$$\tilde{A}_{ij} = \partial \tilde{u}_i/\partial x_j \tag{4.3}$$

is calculated by central finite differences. The resolved rate-of-strain elements are

$$\tilde{S}_{ij} = \tfrac{1}{2}(\tilde{A}_{ij} + \tilde{A}_{ji}). \tag{4.4}$$

During the analysis process, adverse end effects are eliminated by not including strips of width $\Delta/2$ along the boundaries.

4.2. *Time evolution of SGS stresses*

Figure 8 shows several instantaneous realizations of τ_{11} at different times at a filter size of $\Delta/\eta = 30$. In these contour plots it is quite apparent that the SGS stress is intensified during the straining. Also, the contours corresponding to intermediate stresses appear to become slightly more elongated in the extending (x_2) direction.

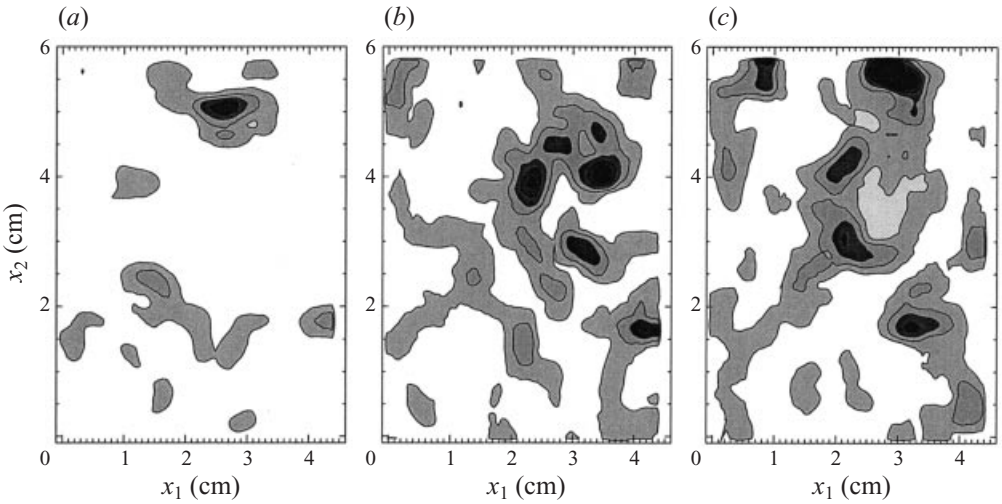

FIGURE 8. Contour plots of SGS stress τ_{11} at different times. The filter scale is $\Delta/\eta = 30$. (*a*) $tS^* = 0$, (*b*) $tS^* = 1.30$, (*c*) $tS^* = 2.09$.

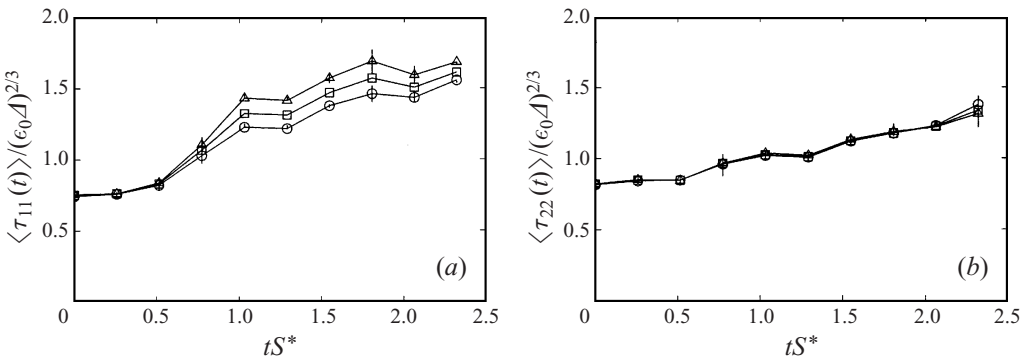

FIGURE 9. Time evolution of mean SGS stresses normalized by the filter size and energy dissipation, according to the Kolmogorov scaling of the SGS stress. (*a*) $\langle\tau_{11}\rangle$, (*b*) $\langle\tau_{22}\rangle$. Vertical bars join results obtained from the first six and last six images, and give an indication of the level of statistical convergence. Circles: $\Delta/\eta = 20$, squares: $\Delta/\eta = 40$, triangles: $\Delta/\eta = 60$.

Figures 9(*a*) and 9(*b*) show the evolution of the mean normal SGS stresses ($\langle\tau_{12}\rangle \sim 0$ due to the symmetry of the flow, and is not shown). The results are normalized by $(\epsilon_0\Delta)^{2/3}$, the inertial-range Kolmogorov scaling for the SGS stress; ϵ_0 is the energy dissipation at the initial stage, as estimated in § 3. The average stresses are evaluated over the entire sample area and the 10 realizations. In order to indicate the degree of statistical convergence, figure 9 includes vertical bars. Their extreme points are determined by averaging the first six samples ($k = 1, 2, \ldots, 6$) and the last six samples ($k = 5, 6, \ldots, 10$). Before straining, $\langle\tau_{11}\rangle$ and $\langle\tau_{22}\rangle$ are similar in magnitude, since the turbulence is nearly isotropic. Consistent with the Kolmogorov scaling, different scales collapse to the same value. When the straining starts, $\langle\tau_{11}\rangle$ becomes scale-dependent, but $\langle\tau_{22}\rangle$ does not. To understand these trends, it is useful to decompose the velocity field into a turbulence part and the applied straining part according to

$$u_i(\boldsymbol{x}, t) = u_i^{(T)}(\boldsymbol{x}, t) + U_i(\boldsymbol{x}, t), \tag{4.5}$$

where $U_i(\boldsymbol{x},t)$ is defined in (3.6). Based on this decomposition, we can separate the SGS stress into three parts: turbulence part, cross-term and the applied straining part, as follows:

$$\tau_{ij}(\boldsymbol{x},t) = \tau_{ij}^{(T)}(\boldsymbol{x},t) + \tau_{ij}^{(C)}(\boldsymbol{x},t) + \tau_{ij}^{(M)}(\boldsymbol{x},t), \tag{4.6}$$

where

$$\tau_{ij}^{(T)}(\boldsymbol{x},t) = \widetilde{u_i^{(T)}u_j^{(T)}} - \tilde{u}_i^{(T)}\tilde{u}_j^{(T)} \tag{4.7}$$

is the turbulence SGS stress. The second part,

$$\tau_{ij}^{(C)}(\boldsymbol{x},t) = \left(\widetilde{u_i^{(T)}U_j} - \tilde{u}_i^{(T)}\tilde{U}_j\right) + \left(\widetilde{U_i u_j^{(T)}} - \tilde{U}_i\tilde{u}_j^{(T)}\right) \tag{4.8}$$

is the cross-term which represents direct interactions between the applied straining and the turbulence. The third part

$$\tau_{ij}^{(M)}(\boldsymbol{x},t) = \widetilde{U_iU_j} - \tilde{U}_i\tilde{U}_j = \frac{\Delta^2}{12}\frac{\partial U_i}{\partial x_m}\frac{\partial U_j}{\partial x_m} \tag{4.9}$$

is caused by the mean strain. Since the mean rate of strain is spatially uniform, $\tau_{ij}^{(M)}$ is also uniform. It can be expressed in terms of the applied straining according to

$$\tau_{11}^{(M)}(t) = \frac{\Delta^2}{12}\left\langle\tilde{S}_{11}\right\rangle^2, \tau_{22}^{(M)}(t) = \frac{\Delta^2}{12}\left\langle\tilde{S}_{22}\right\rangle^2, \tau_{12}^{(M)}(t) = 0. \tag{4.10}$$

The relative effect of each term on the total stress for different Δ is shown in figure 10. The plots contain averages of the absolute values in order to include information about the cross-term which vanishes on average. The magnitudes of the turbulent stresses scale like $\langle|\tau^{(T)}|\rangle \sim \Delta^{2/3}$, which is compatible with Kolmogorov scaling, and agrees with the results of Liu *et al.* (1995) for unstrained turbulence. Thus, the applied straining does not have a significant impact on the scaling of the turbulent SGS stress. The cross-parts scale approximately like $\langle|\tau^{(C)}|\rangle \sim \Delta$, a trend for which we have no explanation. As can be expected from (4.10), the straining part scales as $\langle|\tau^{(M)}|\rangle \sim \Delta^2$. It is evident from figure 10 that at large scales, $\langle\tau_{11}^{(M)}\rangle$ and $\langle|\tau_{11}^{(C)}|\rangle$ become comparable to the turbulent stress. Thus, in the present range of Δ, $\langle\tau_{11}^{(M)}\rangle$ is sufficiently large to modify trends in the total stress (see figure 9*a*). As will be seen in the following sections, $\tau_{ij}^{(C)}$ and $\tau_{ij}^{(M)}$ also have considerable impact on the energy dissipation from resolved to subgrid scales. Conversely, in the 22-component, the mean and cross- terms are considerably smaller than the turbulence stress, since $\langle S_{22}\rangle^2 = \frac{1}{4}\langle S_{11}\rangle^2$. Consistent with figure 9*b*, the normalized $\langle\tau_{22}\rangle$ does not vary much with scale.

4.3. *Rapid distortion theory*

As outlined in § 1.2, RDT has been used in the past to predict the time evolution of Reynolds stresses when the applied straining S^* was very large compared to the turbulent large-scale strain. Here, RDT is used to predict the short-time evolution of the mean SGS stresses instead of the Reynolds stresses. The ensemble-average turbulent SGS stress can be written as

$$\langle\tau_{ij}^{(T)}\rangle = \langle\widetilde{u_i^{(T)}u_j^{(T)}}\rangle - \langle\tilde{u}_i^{(T)}\tilde{u}_j^{(T)}\rangle = \widetilde{\langle u_i^{(T)}u_j^{(T)}\rangle} - \langle\tilde{u}_i^{(T)}\tilde{u}_j^{(T)}\rangle \tag{4.11}$$

since filtering and averaging commute. Next, for homogeneous turbulence, $\langle u_i^{(T)}u_j^{(T)}\rangle$ is uniform in space. Then $\widetilde{\langle u_i^{(T)}u_j^{(T)}\rangle} = \langle u_i^{(T)}u_j^{(T)}\rangle$ is equal to the Reynolds stress. On

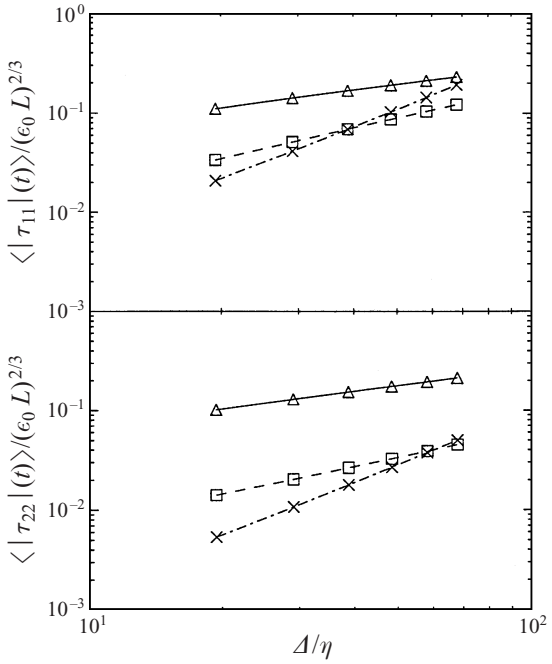

FIGURE 10. Magnitude of different SGS stress terms as a function of filter size, at $tS^* = 2.34$. Triangles: turbulent stress, squares: cross-stress, crosses: mean straining part. Results are normalized with the large-scale velocity $(\epsilon_0 L)^{1/3}$, where L is the integral scale.

the other hand, we can write

$$\langle \tilde{u}_i^{(T)} \tilde{u}_j^{(T)} \rangle = \int |\hat{F}_\Delta(\boldsymbol{k})|^2 \Phi_{ij}(\boldsymbol{k}, t) \mathrm{d}\boldsymbol{k}^3, \tag{4.12}$$

where $\hat{F}_\Delta(\boldsymbol{k})$ is the filter's Fourier transform (in the case of the experimental data a two-dimensional filter), and $\Phi_{ij}(\boldsymbol{k}, t)$ is the spectral tensor of the turbulent velocity field. Therefore,

$$\langle \tau_{ij}^{(T)} \rangle = \int (1 - |\hat{F}_\Delta(\boldsymbol{k})|^2) \Phi_{ij}(\boldsymbol{k}, t) \mathrm{d}^3\boldsymbol{k}. \tag{4.13}$$

Using the RDT expression for $\Phi_{ij}(\boldsymbol{k}, t)$ of Lee (1989) for axisymmetric expansion, and using a two-dimensional filter expression for $\hat{F}_\Delta(\boldsymbol{k})$, the mean turbulence SGS stress can be evaluated. While the experimental data are analysed using a top-hat filter, the integration in wavespace is greatly simplified if a spectral cutoff filter is used. Since one does not expect significant discrepancies in the mean stress to arise from different filter shapes, we use the cutoff filter. We first consider the case of three-dimensional filtering and then proceed to two-dimensional filtering. The spherical cutoff filter in Fourier space for three-dimensional filtering is given by

$$|\hat{F}_\Delta(\boldsymbol{k})|^2 = \begin{cases} 1 & \text{if } |\boldsymbol{k}| \leqslant \pi/\Delta \\ 0 & \text{otherwise.} \end{cases} \tag{4.14}$$

Using spherical coordinates, the SGS stress is given by

$$\left\langle \tau_{ij}^{(T)} \right\rangle_{3D}(t) = \int_{\pi/\Delta}^{\infty} \mathrm{d}k \int_0^{\pi} \mathrm{d}\theta \int_0^{2\pi} \mathrm{d}\phi \, \Phi_{ij}(\boldsymbol{k}, t). \tag{4.15}$$

For rapid axisymmetric expansion, equation (3.5), the short-time evolution of $\Phi_{ij}(\boldsymbol{k},t)$ is given in Lee (1989), and expressed as function of the accumulated applied straining

$$c(t) = \exp\left(\int_0^t S(t')\mathrm{d}t'\right). \tag{4.16}$$

The results are

$$\Phi_{11}(\boldsymbol{k},t) = \frac{E(k)}{4\pi}\frac{c^2(k_2^2+k_3^2)}{(c^3k_1^2+k_2^2+k_3^2)^2}, \tag{4.17}$$

$$\Phi_{22}(\boldsymbol{k},t) = \frac{E(k)}{4\pi}\frac{c^{-1}\left((c^6k_2^2+k_3^2)-(1-c^3)^2k_1^2k_3^2/k^2\right)}{(c^3k_1^2+k_2^2+k_3^2)^2}, \tag{4.18}$$

and

$$\Phi_{12}(\boldsymbol{k},t) = -\frac{E(k)}{4\pi}\frac{c^7k_1k_2}{(c^3k_1^2+k_2^2+k_3^2)^2}, \tag{4.19}$$

where $E(k)$ is the energy spectrum of isotropic turbulence at $t=0$, and $k=|\boldsymbol{k}|$. These results are substituted in (4.15) with k_1 as the axial direction, and $a \equiv c^3-1$. The radial integration factors out (see e.g. Batchelor & Proudman 1954; Lee 1989) and one obtains the same result as for Reynolds stresses, up to a dimensional prefactor:

$$\left\langle\tau_{11}^{(T)}\right\rangle_{3D}(t) = c_K\ \pi^{-2/3}\ \tfrac{3}{4}(\epsilon\Delta)^{2/3}\frac{(a+1)^{2/3}}{a}\left(1+\frac{a-1}{a^{1/2}}\arctan a^{1/2}\right), \tag{4.20}$$

$$\left\langle\tau_{22}^{(T)}\right\rangle_{3D}(t) = c_K\ \pi^{-2/3}\ \tfrac{3}{8}(\epsilon\Delta)^{2/3}\frac{(a+1)^{5/3}}{a}\left(\frac{1}{a^{1/2}}\arctan a^{1/2}+\frac{a-1}{(a+1)^2}\right); \tag{4.21}$$

$\langle\tau_{12}^{(T)}\rangle(t)=0$ at all times. We have used the Kolmogorov spectrum for $E(k)$, but since the radial integration factors out, the ratio $\langle\tau_{11}^{(T)}\rangle_{3D}(t)/\langle\tau_{11}^{(T)}\rangle_{3D}(0)$ is independent of the shape of the radial spectrum, and equals that of the Reynolds stresses (Lee 1989).

In the two-dimensional filtering process used for the two-dimensional experimental data, the filtering is performed only in the x_1- and x_2-directions with a box filter. This process is approximated here with a cylindrical cutoff filter. Now the axial direction is taken in the k_3-direction (perpendicular to the data plane), and the SGS stresses can be written as

$$\langle\tau_{ij}^{(T)}\rangle_{2D}(t) = \int_0^{\pi} d\theta \int_{\pi/(\Delta\sin\theta)}^{\infty}\mathrm{d}k\int_0^{2\pi}\mathrm{d}\phi\,\Phi_{ij}(\boldsymbol{k},t). \tag{4.22}$$

Replacing the RDT spectra (4.17)–(4.17) and the Kolmogorov radial spectrum for the initial condition, both the k and ϕ integrations can be done analytically. The result is

$$\langle\tau_{11}^{(T)}\rangle_{2D}(t) = c_K\pi^{-2/3}\tfrac{3}{8}(\epsilon\Delta)^{2/3}(1+a)^{2/3}\int_0^{\pi}\sin^{5/3}\theta\frac{2+(a-1)\sin^2\theta}{(1+a\sin^2\theta)^{3/2}}\mathrm{d}\theta, \tag{4.23}$$

$$\langle\tau_{22}^{(T)}\rangle_{2D}(t) = c_K\pi^{-2/3}\tfrac{3}{8}(\epsilon\Delta)^{2/3}(1+a)^{-1/3} \times\int_0^{\pi}\sin^{5/3}\theta\frac{a(a-1)\sin^4\theta+(3a-1)\sin^2\theta+2}{(1+a\sin^2\theta)^{3/2}}\mathrm{d}\theta, \tag{4.24}$$

and $\langle\tau_{12}^{(T)}\rangle_{2D}(t)=0$. Notice that here the radial integration does not factor out, so this result is limited to an inertial-range energy spectrum. The θ-integrals are computed

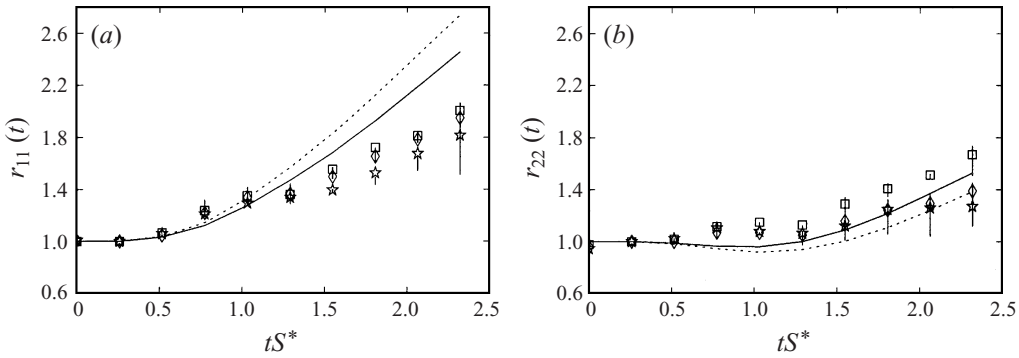

FIGURE 11. Comparison of normalized SGS stresses (symbols) computed according to (4.25) and averaged over ten vector fields, with RDT prediction (lines) for the 11-component (*a*) and the 22-component (*b*). Vertical bars join results obtained from the first and last six fields. Solid lines are for two-dimensional filtered RDT results, dotted lines are three-dimensional filtered RDT results. Squares: $\Delta/\eta = 30$, rhombs: $\Delta/\eta = 50$, stars: $\Delta/\eta = 280$.

by numerical integration using *Mathematica*^{TM}; $a(t) = c(t)^3 - 1$, where $c(t)$ is obtained from (4.16) with $S(t)$ replaced by the measured mean strain magnitude, $|\langle S_{11}(t')\rangle|$ (see figure 7). The trapezoidal rule is used for the time integration. Results are compared with measurements in the next section.

4.4. *Experimental results vs. RDT prediction*

The turbulence SGS stresses $\langle\tau_{11}\rangle$ and $\langle\tau_{22}\rangle$ are computed from the data by averaging over all points of an image, and are normalized by their values at $t_0 = 0.03\,\mathrm{s}$, taken here as the initial reference time. The ratios are then averaged over all the 10 realizations available for the same time,

$$r_{ij}(t) = \left\langle \frac{\langle \tau_{ij}^{(T)}(t)\rangle_a}{\langle \tau_{ij}^{(T)}(t_0)\rangle_a} \right\rangle_b, \tag{4.25}$$

where $\langle . \rangle_a$ indicates a spatial average over each image, and $\langle . \rangle_b$ refers to ensemble averaging over all images. This process is repeated for different filter sizes, $\Delta/\eta =$ 280, 80, 40, and 20. The results are compared to the two-dimensional filtered RDT prediction (solid lines) in figures 11(*a*) and 11(*b*). Dashed lines are the RDT prediction using a three-dimensional radial filter, which is equivalent to the classical result (see Lee 1989). Vertical bars indicate, as in figure 9, convergence uncertainty by displaying the results from the first six and last six experiments. Both r_{11} and r_{22} increase more rapidly at small scales than at large scales. The results fall below the RDT line for the 11-component, and around the RDT line for the 22-component. In other words, the results are more isotropic than the RDT prediction. In figure 11(*a*), r_{11} is closer to the RDT line at small scales than at larger filter scales. Conversely, in figure 11(*b*) it appears that r_{22} falls closer to the RDT line at large scales. While we do not have an explanation for such an effect, it must be recognized that the error bars are significant at the later times.

In order to directly assess the isotropy of the SGS stress tensor, we cast the results in terms of the anisotropy tensor, b_{ij}, where

$$b_{ij} = \frac{r_{ij}}{r_{kk}} - \tfrac{1}{3}\delta_{ij}. \tag{4.26}$$

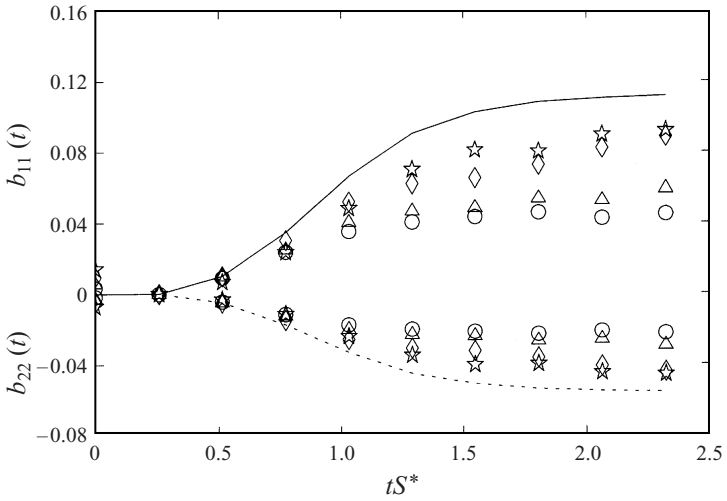

FIGURE 12. Anisotropy tensor b_{ij} of normalized stress r_{ij}. Solid line and upper set of symbols: 11-component; dashed line and lower set of symbols: 22-component. Stars: $\Delta/\eta = 280$, rhombs: $\Delta/\eta = 80$, triangles: $\Delta/\eta = 40$, circles: $\Delta/\eta = 20$; lines: two-dimensional filtered RDT prediction.

The trace, r_{kk}, can be obtained from the experimental data by assuming that $r_{33} = r_{22}$ due to axisymmetry. As shown in figure 12, b_{ij} becomes increasingly more isotropic with decreasing scale. However, even at the largest scale considered (280η), b_{ij} is still less anisotropic than the RDT prediction. To verify that these results are not influenced by the noise present at the smallest scales (see figure 4), which could increase isotropy, several filtering operations that remove the noise floor are applied to the data. Analysis based on these filtered data (not shown) yields almost identical SGS stresses and trends.

From the discussion above, one can conclude that during rapid straining, the small scales remain more isotropic than the large ones, i.e. deviate more from the RDT prediction. This trend is not surprising if one estimates the characteristic time scale for eddies of size Δ as $T_\Delta = \epsilon_o^{-1/3}\Delta^{2/3}$. For the smallest filter-scale considered the time scale is $T_{\Delta=20\eta} = 0.15\,\mathrm{s}$. This value is already on the order of the inverse time scale of the applied strain rate, $1/S^* = 0.12\,\mathrm{s}$. Thus, the basic assumption of RDT ($1/S^* \ll T_\Delta$) does not hold for the smaller scales in this flow.

It should be pointed out that for *Reynolds stresses* undergoing *slow* axisymmetric expansion, anisotropy larger than the RDT prediction has been observed in the past (Choi 1983; Lee 1985). Since the distortion applied in our experiment is slow relative to the time scale of the small scales, there is an apparent contradiction. To understand possible causes for the different trends, note that average SGS stresses and Reynolds stresses are variables whose evolution equations differ substantially. Among others, it is simple to show that the evolution equation for the mean SGS stress contains production terms of the form $\langle \tau_{ik}^{(T)} \partial \tilde{u}_j^{(T)} / \partial x_k \rangle$, which have no analogue in the Reynolds stress equation. Differences also exist in the pressure–strain correlation terms.

We have attempted to compute the Reynolds stresses from the unfiltered data during straining in order to directly compare the behaviour of SGS and Reynolds stresses in the present data. Unfortunately, only ten vector maps are available at each time during the straining (as opposed to 20 for the initial turbulence). Furthermore, as can be seen in figure 4, the peaks of the spectra at large scales are not resolved. These

limitations cause large variabilities, making it very difficult to identify clear trends. Convergence of the large-scale properties is more difficult than the normalized SGS properties since in the latter case there are more independent events to average over. For SGS stresses there are about $\sim n\,(L/\Delta)^3$ events, where n is the number of vector maps, L is the image size, and Δ the filter size. For the Reynolds stresses there are only about n independent large-scale events. Consequently, results for the unfiltered Reynolds stresses are not presented.

5. Scale similarity during straining

So far, we have focused on the average SGS stress, and its dependence on time and filter scale. This section focuses on the local features of the total SGS stress. In the previous section, the SGS stress was separated into three terms, for the purpose, among others, of comparing them to RDT. However, during LES of complex flows, it is usually impossible to separate the turbulence from the mean, and it is thus common to treat the total SGS stress as one single term that needs to be modelled.

To gain insight about local features of the flow at different scales, in Liu *et al.* (1994) the velocity field was decomposed into several bands of scales. Particular local flow structures were found to be present simultaneously in consecutive bands, which led to the scale-similarity model of (1.4). To ascertain if this 'structure coherence' persists during the rapid straining, this analysis is repeated using the present data. The measured velocity field is decomposed into contributions from separate scale bands, according to

$$u_i(\boldsymbol{x}) = \sum_{n=1}^{N} u_i^{(n)}(\boldsymbol{x}), \tag{5.1}$$

where the velocity field in each band, $u_i^{(n)}(\boldsymbol{x})$, is given by

$$u_i^{(n)}(\boldsymbol{x}) = \tilde{u}_i(\boldsymbol{x}) - \overline{u}_i(\boldsymbol{x}). \tag{5.2}$$

The tilde filtering is at a scale $\Delta = 2^{-n}W$, where W denotes the image width in the x_1-direction ($W \approx 320\eta$) and $n = 1$ to 5. As before, the overbar denotes filtering at a scale $2\Delta = 2^{-(n-1)}W$. To be consistent with information that would be available during LES and to avoid overlap of information, $\tilde{u}_i(\boldsymbol{x})$ is sampled on a grid of size Δ. Bilinear interpolation is employed to generate a smooth field between grid points only for graphical illustration purposes; $\overline{u}_i(\boldsymbol{x})$ is determined from $\tilde{u}_i(\boldsymbol{x})$, but it is sampled on a coarser grid of spacing $2\Delta = 2^{-(n-1)}W$. Again, a smooth field is generated by bilinear interpolation.

Figure 13 is the band velocity field for $n = 3$ and 4 prior to straining, when the turbulence is still nearly isotropic. The structure coherence is evident, i.e. a number of common features can be observed in both plots (e.g. the highlighted vortical structures). It should be remarked that using wavelet analysis of two-dimensional turbulence, Farge & Rabreau (1988) also found significant correlation between scales for coherent structures. Figure 14 displays a sequence of band velocity fields at consecutive times during straining. The top figures show the larger scale (band $n = 3$) and the bottom ones display the smaller scale (band $n = 4$). Several qualitative observations can be made from these data. First, by comparing figures 13 and 14, it is quite apparent that the turbulence is intensified in both bands due to the straining. Second, to highlight the time evolution of these fields during straining, attention is drawn to particular flow features, such as a saddle, a node and two 'jetting' regions.

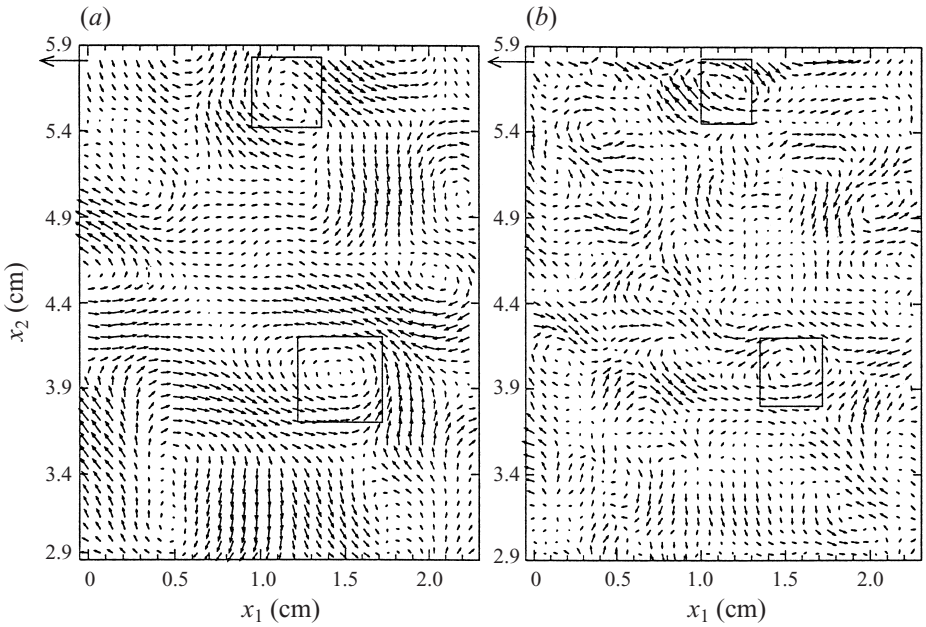

FIGURE 13. The band velocity field at two scales, (*a*) $n = 3$ and (*b*) $n = 4$, at $tS^* = 0$, when the flow is nearly isotropic and homogeneous. A reference vector is plotted on the top-left corner, corresponding to 0.1 m s^{-1}, and vortical structures are highlighted. Only a quarter of the whole field is plotted.

These regions are defined here by visual inspection, as more sophisticated classifications of flow regions, such as by Hunt, Wray & Moin (1988), require knowledge of the three-dimensional local flow-structure. At $tS^* = 1.82$ the chosen regions are surrounded by rectangles. The vertices are then convected by time integration of $\overline{u}_i$. Bilinear interpolations in space and time are employed to evaluate $\overline{u}_i(\boldsymbol{x})$ from the data. As can be seen from the vector maps at successive times (at $n = 3$), some of the highlighted flow features are convected by the two measured components of $\overline{u}_i$, in particular the two jetting regions and the saddle. However, the node is convected at a different velocity, possibly due to the fact that $\overline{u}_3$ is not accounted for. Also, the local flow structures are distorted. These qualitative observations are consistent with what can be deduced from the evolution equation of $u_i^{(n)}$. It is obtained by subtracting the equation for $\overline{u}_i$ from that of $\tilde{u}_i$, and reads

$$\frac{\partial u_i^{(n)}}{\partial t} + \overline{u}_j \frac{\partial u_i^{(n)}}{\partial x_j} = -u_j^{(n)} \frac{\partial \overline{u}_i}{\partial x_j} - \frac{\partial Q_{ij}}{\partial x_j}, \tag{5.3}$$

where $Q_{ij} = (\tilde{p} - \overline{p})/\rho\delta_{ij} - \tau_{ij} + T_{ij} + u_i^{(n)}u_j^{(n)}$, and T_{ij} is the SGS stress at scale 2Δ. According to (5.3), the band velocity $u_i^{(n)}$ is convected by $\overline{u}_i$, but is also distorted (stretched and tilted) by $\partial\overline{u}_i/\partial x_j$ and affected by the transport term Q_{ij}. The distortion term $-u_j^{(n)}\partial\overline{u}_i/\partial x_j$ vanishes for critical points where $u_i^{(n)} = 0$ (such as the saddles and nodes). But, they can still be affected by $\partial Q_{ij}/\partial x_j$. Thus, we expect considerable changes in the local flow structure as it is convected by the larger scales.

The third observation involves comparing data filtered at two consecutive scales. Structures that appear at the larger scale are likely to appear also in the smaller scales. For example, at $tS^* = 2.09$, a 'vortex' at $x_1 \sim 0.25$ cm and $x_2 \sim 3.5$ cm is

https://doi.org/10.1017/S0022112099004504 Published online by Cambridge University Press

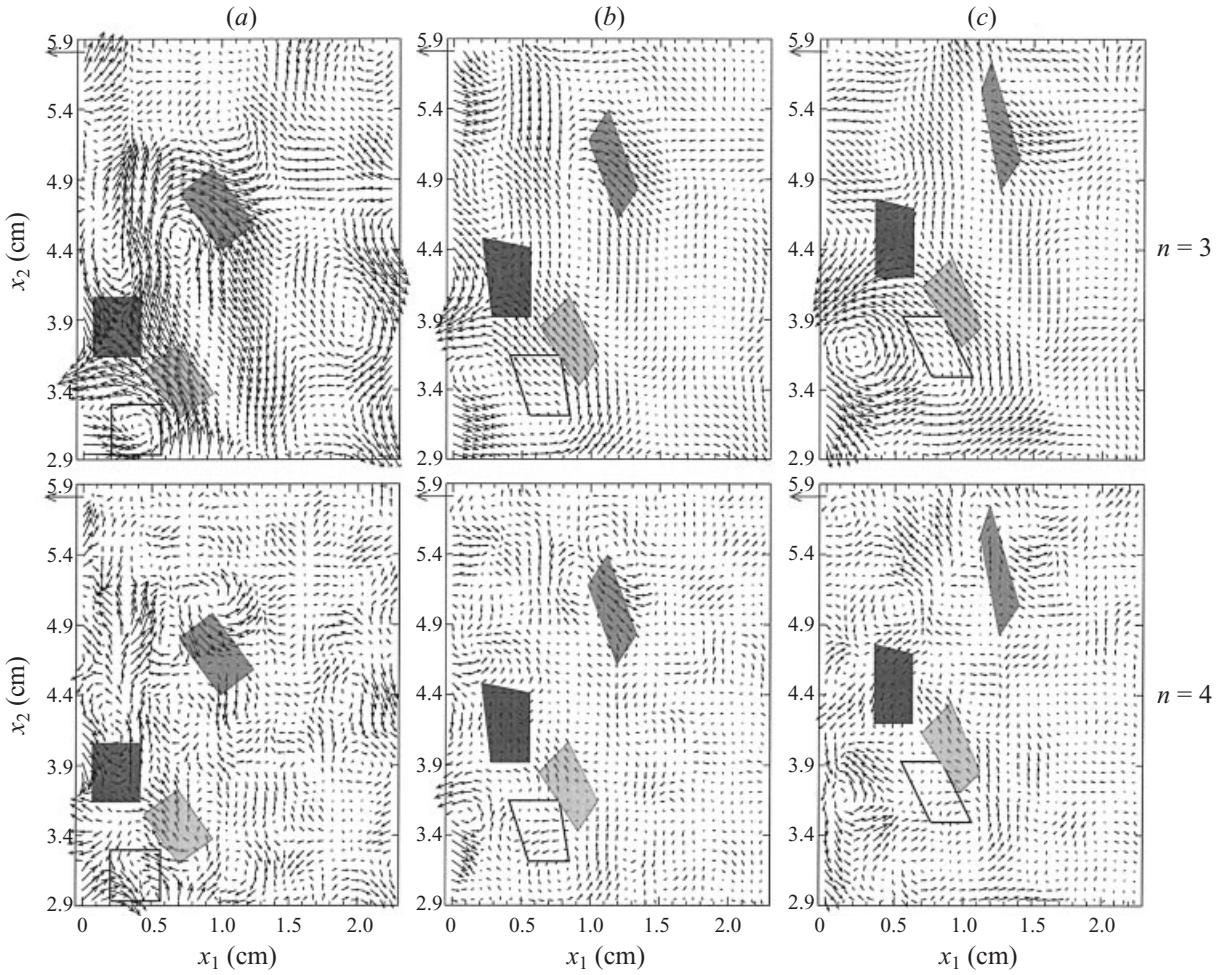

FIGURE 14. The band velocity field at different times during straining ((*a*) $tS^* = 1.82$, (*b*) $tS^* = 2.09$, (*c*) $tS^* = 2.36$). The reference vector is 0.1 m s^{-1}. Only a quarter of the whole field is plotted. Vertices of shaded regions are convected by the large-scale velocity field $\bar{\boldsymbol{u}}$ (with $n = 3$). The same shadings refer to the same fluid elements.

clearly evident at both scales. So is the jetting region at $x_1 \sim 1.1$ cm and $x_2 \sim 5.1$ cm. There are many other similar examples (but some counter examples as well). Thus, it appears that the coherence between turbulent structures at different scales persists during the straining process. This means that the foundation for the similarity model, as described in Liu *et al.* (1994), should also apply to turbulence under rapid straining. Following the same logic, for a filter scale Δ one can argue that the real SGS stress, τ_{ij}, is dominated by the velocity in band n. The resolved stress, L_{ij}, is dominated by the velocity in band $n-1$. Given the similarity in the velocity fields, there should also be similarity between τ_{ij} and L_{ij}.

Next, τ_{ij} and L_{ij} are compared quantitatively during rapid straining. As in Liu *et al.* (1994), special care is taken in how L_{ij} is computed. In order to use only information that would be available for LES computations on a grid with scale Δ, $\tilde{u}_i$ is coarsely sampled on such a grid (i.e. the velocity in a cell of size Δ is replaced by its average in that cell) before the second filtering is performed. Such a procedure effectively renders the small-scale field (the difference between the real and the piecewise-constant large-scale field) orthogonal to the large-scale field, eliminating any trivial overlap of information between resolved and subgrid scales. When evaluating L_{ij} the planar filtering at scale 2Δ of a coarse-grained variable $\tilde{a}$ is performed according to

$$\begin{aligned}\bar{\tilde{a}}_{(m,n)} = {} & \tfrac{1}{4}\tilde{a}_{(m,n)} + \tfrac{1}{8}\left[\tilde{a}_{(m+1,n)} + \tilde{a}_{(m-1,n)} + \tilde{a}_{(m,n+1)} + \tilde{a}_{(m,n-1)}\right] \\ & + \tfrac{1}{16}\left[\tilde{a}_{(m+1,n+1)} + \tilde{a}_{(m-1,n+1)} + \tilde{a}_{(m+1,n-1)} + \tilde{a}_{(m-1,n-1)}\right], \end{aligned} \tag{5.4}$$

where $\tilde{a}_{(m,n)}$ is the variable at node (m,n) ($\tilde{a}$ can be $\tilde{u}_i$ or $\tilde{u}_i\tilde{u}_j$), and the distance between nodes is Δ.

Traditional *a priori* tests have often employed correlation coefficients to quantify the local agreement between real and modeled SGS stresses. The correlation coefficient between two variables a and b is defined as usual:

$$\rho(a,b) = \frac{\langle ab\rangle - \langle a\rangle\langle b\rangle}{(\langle a^2\rangle - \langle a\rangle^2)^{1/2}(\langle b^2\rangle - \langle b\rangle^2)^{1/2}}. \tag{5.5}$$

Figure 15(a) shows the time evolution of the correlation coefficients between the real stress and the similarity model for $\Delta/\eta \sim 30$. The correlation coefficient is computed separately for each tensor element, i.e. $\rho(\tau_{\alpha\beta}, \tau^{\mathrm{mod}}_{\alpha\beta})$, with no summation over indices since for the present application not all tensor elements are known. The figure shows that the correlation coefficients are essentially constant throughout the straining process, for all measured tensor components. Again, the vertical bars denote the variability in convergence as defined in the previous figures. Tests at different Δ (not shown) yield similar correlations. The relatively elevated value of the correlation throughout the straining confirms the qualitative observations about scale coherence. Next, the correlations associated with the Smagorinsky model are considered. Since the model only attempts to reproduce the deviatoric part of the stress, we must correlate the Smagorinsky prediction to $(\tau_{ij} - \frac{1}{3}\tau_{kk}\delta_{ij})$. However, since τ_{33} is not measured, we substitute $\tau_{33} = \tau_{22}$ locally. Then, the 11-component of the Smagorinsky model is compared to $\frac{2}{3}\tau_{11} - \frac{2}{3}\tau_{22}$, and the 22-component to $\frac{1}{3}\tau_{22} - \frac{1}{3}\tau_{11}$. The results are also plotted in figure 15(a) (dashed lines). During the isotropic turbulence phase before straining, the correlation is very low (below 0.2) for all three components, consistent with previous results (Clark *et al.* 1979; Liu *et al.* 1994, etc.). During straining, the correlation for the 11- and 22-components increases slightly, while the correlation for the 12-component remains low. They are still lower than results for the similarity model.

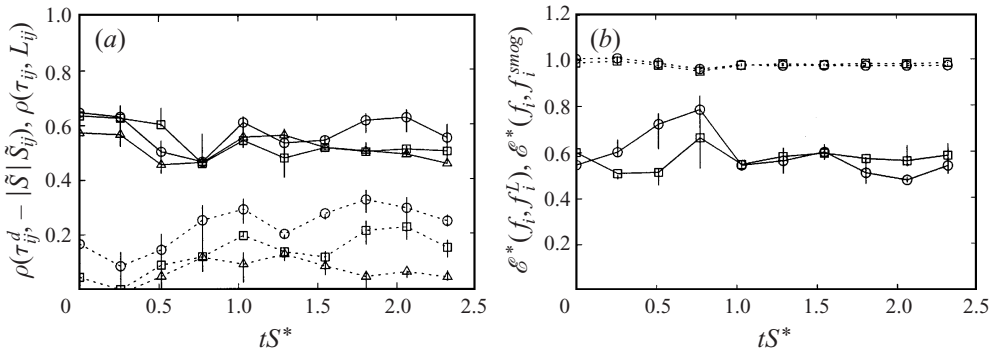

FIGURE 15. (*a*) Correlation coefficients between SGS stress and similarity (symbols and solid lines), and Smagorinsky model (symbols and dotted lines). Circles: 11-component, squares: 22-component, triangles: 12-component. The filter-scale is $\Delta/\eta = 30$. Very similar results are obtained at other filter scales. Vertical bars join results obtained from the first and last six vector maps. (*b*) Global square-error between real and modelled SGS force. Similarity model: symbols and lines, Smagorinsky model: symbol and dotted lines. Circles: f_1 component; Squares: f_2 component.

Adrian (1990) and, more recently, Moser & Adrian (1998) show that for a LES to reproduce the short-time evolution of the large scales, it is of interest to consider the square-error

$$\mathscr{E}(f_\alpha, f_\alpha^{\mathrm{mod}}) = \left\langle (f_\alpha - f_\alpha^{\mathrm{mod}})^2 \right\rangle, \tag{5.6}$$

where f_i and f_i^{mod} are the real and modeled SGS force, respectively. The SGS force is defined as the divergence of the SGS stress, i.e. $f_i = \partial\tau_{ij}/\partial x_j$. Adrian (1990) and Moser & Adrian (1998) point out the interesting fact that the least-square-error is achieved if a model reproduces the conditional average $\langle f_i | \boldsymbol{V}_1, \boldsymbol{V}_2, \ldots \boldsymbol{V}_N \rangle$, where $\{\boldsymbol{V}_1, \boldsymbol{V}_2, \ldots \boldsymbol{V}_N\}$ represents a given configuration of the entire velocity field at all (N) points in the flow. Moreover, this condition is sufficient for LES to reproduce the entire multipoint p.d.f. of the resolved scales (S. B. Pope 1997, personal communication). Interestingly, it thus closes the hierarchy of statistical conditions derived in Meneveau (1994) which were necessary, but not sufficient, conditions at any finite order of moments. However, since the conditioning is based on an entire multipoint configuration of the resolved velocity field, tests for $\langle f_i | \boldsymbol{V}_1, \boldsymbol{V}_2, \ldots \boldsymbol{V}_N \rangle$ are not easily performed in practice without resorting to a number of assumptions. Nevertheless, models can be compared more simply on the basis of their ability to reduce the global error $\mathscr{E}(f_\alpha, f_\alpha^{\mathrm{mod}})$. Models for which $\mathscr{E}(f_\alpha, f_\alpha^{\mathrm{mod}})$ is smaller will be closer to an optimal SGS model.

The SGS force cannot be computed from the planar data since gradients and tensor elements in the x_3-direction are unavailable. Thus, in the present study only two terms of the stress divergence are used for the comparison,

$$f_1^{2D} = \frac{\partial\tau_{11}}{\partial x_1} + \frac{\partial\tau_{12}}{\partial x_2}, \quad f_2^{2D} = \frac{\partial\tau_{12}}{\partial x_1} + \frac{\partial\tau_{22}}{\partial x_2}. \tag{5.7}$$

The differentiation is performed using centred finite differences on the coarse mesh of size Δ, and the error is computed according to (5.6). To properly scale the results, the error $\mathscr{E}(a, b)$ is normalized as follows:

$$\mathscr{E}^*(a, b) = \frac{\mathscr{E}(a, b)}{\sigma_a^2 + \sigma_b^2 + (\langle a \rangle - \langle b \rangle)^2}, \tag{5.8}$$

where σ_a^2 and σ_b^2 are the variances of a and b, respectively. It is simple to show that

the normalized error and the correlation coefficient $\rho(a,b)$ are related according to

$$\mathscr{E}^*(a,b) = 1 - \frac{2\sigma_a\sigma_b}{\sigma_a^2 + \sigma_b^2 + (\langle a\rangle - \langle b\rangle)^2}\ \rho(a,b), \tag{5.9}$$

so that if both variables a and b have the same mean and variance, $\mathscr{E}^* = 1-\rho$. Otherwise, $\mathscr{E}^* > 1-\rho$.

Figure 15(b) shows the time evolution of the normalized error for the Smagorinsky model and the similarity model. As can be seen, the error is almost the maximum value near 1 for the Smagorinsky model (this is consistent with recent DNS results for isotropic turbulence (R. D. Moser 1998, personal communication)). This large error is related to two effects: (i) the correlation between the real and Smagorinksy SGS force is low (we obtain typical values around $\rho(f_i^{2D}, f_i^{2D^{\mathrm{smag}}}) \sim 0.3$), and (ii) the variances differ significantly (see Liu *et al.* 1995). The error for the similarity force is about $\mathscr{E}^*(f_i^{2D}, f_i^{2D^{\mathrm{sim}}}) \sim 0.6$, smaller than that of the Smagorinsky model although still large.

We conclude that both criteria, the correlation coefficient and the square-error, indicate that the similarity model is a relative improvement over the Smagorinsky model for both strained and unstrained turbulence. This conclusion is valid for the box filter. As in Liu *et al.* (1994), analysing the data using a spectral cutoff filter leads to very low correlation coefficients (and thus large errors) for the similarity model. Although the spectral filter's long tail in physical space introduces significant errors due to boundary effects, we believe this conclusion is correct as it agrees with previous findings from DNS (Meneveau, Lund & Moin 1993).

6. SGS energy dissipation and model coefficients

Probably the most important feature of the SGS stress is that it interacts with the large scales to exchange, and typically dissipate, kinetic energy on average. In this section, we focus on averaged and localized features of the SGS dissipation during rapid straining. We also evaluate the coefficients in the Smagorinsky and similarity models by balancing the real and modelled SGS dissipation.

6.1. *Subgrid energy dissipation*

Neglecting the viscous terms, the evolution equation for mean resolved kinetic energy reads

$$\frac{\partial}{\partial t}\left\langle \tfrac{1}{2}\tilde{u}_i^2\right\rangle + \langle\tilde{u}_j\rangle \frac{\partial}{\partial x_j}\left\langle \tfrac{1}{2}\tilde{u}_i^2\right\rangle = -\frac{\partial}{\partial x_j}\left(\left\langle \tilde{u}_j \tfrac{1}{2}\tilde{u}_i^2\right\rangle - \langle\tilde{u}_j\rangle\left\langle \tfrac{1}{2}\tilde{u}_i^2\right\rangle \langle\tilde{p}\tilde{u}_j\rangle + \langle\tilde{u}_i\tau_{ij}\rangle\right) + \left\langle \tau_{ij}\tilde{S}_{ij}\right\rangle. \tag{6.1}$$

It shows that the SGS stress affects the mean kinetic energy through two mechanisms: the transport term $\langle\tilde{u}_i\tau_{ij}\rangle$ and the dissipation term $\Pi(t) \equiv -\left\langle\tau_{ij}\tilde{S}_{ij}\right\rangle$. For typical, near-equilibrium flows in which turbulent strains at scale Δ are larger than the mean velocity gradients, the SGS dissipation becomes increasingly dominant over the transport term as Δ decreases. Since the two terms scale differently with Δ, they are usually considered separately, and most attention is given to the dissipation term, $\Pi(t)$. Thus, we shall also focus on $\Pi(t)$, its time evolution and modeling. In general, the dissipation term consists of two contributions:

$$\left\langle\tau_{ij}\tilde{S}_{ij}\right\rangle = \left\langle\tau_{ij}\right\rangle\left\langle\tilde{S}_{ij}\right\rangle + \left\langle\tau_{ij}\tilde{S}_{ij}^{(T)}\right\rangle, \tag{6.2}$$

where $\tilde{S}_{ij}^{(T)} = \tilde{S}_{ij} - \langle\tilde{S}_{ij}\rangle$ is the fluctuating part of the resolved strain-rate tensor.

Since during rapid straining, $\langle \tilde{S}_{ij} \rangle$ is typically as large as, or larger than $\tilde{S}_{ij}^{(T)}$, we expect the first term to contribute significantly to the total dissipation. However, for the present case of rapid straining of homogeneous turbulence, $\langle \tau_{ij} \rangle \langle \tilde{S}_{ij} \rangle$ is exactly balanced by the term $(\partial/\partial x_j)\langle \tilde{u}_i \tau_{ij} \rangle = (\partial/\partial x_j)\langle \tilde{u}_i^{(T)} \tau_{ij} \rangle + \langle \tau_{ij} \rangle \langle \tilde{S}_{ij} \rangle = \langle \tau_{ij} \rangle \langle \tilde{S}_{ij} \rangle$, since $\langle \tilde{u}_i^{(T)} \tau_{ij} \rangle$ is spatially uniform for homogeneous turbulence. Thus, for homogeneous turbulence, the net effect of τ_{ij} on the resolved kinetic energy can be expressed by the net dissipation term

$$\Pi^*(t) = -\langle \tau_{ij} \tilde{S}_{ij}^{(T)} \rangle \tag{6.3}$$

involving only the fluctuating strain rate. Therefore, we also consider the behaviour of $\Pi^*(t)$.

6.2. *Assumption of subgrid axisymmetry and simplifications*

One frequently needs to evaluate the contraction of two tensors, such as the SGS dissipation, the strain-rate magnitude $|\tilde{S}| = (2\tilde{S}_{ij}\tilde{S}_{ij})^{1/2}$, etc. Unfortunately, the two-dimensional PIV data provide only two velocity components, u_1 and u_2, and three tensor components of the rate of strain, $\tilde{S}_{11}$, $\tilde{S}_{22}$, $\tilde{S}_{12}$, and SGS stress, τ_{11}, τ_{22}, τ_{12}. Therefore, certain assumptions and approximations have to be made in order to evaluate the tensor contractions. For example

$$\langle \tau_{ij}\tilde{S}_{ij} \rangle = \langle \tau_{11}\tilde{S}_{11} \rangle + \langle \tau_{22}\tilde{S}_{22} \rangle + \langle \tau_{33}\tilde{S}_{33} \rangle + 2\left(\langle \tau_{12}\tilde{S}_{12} \rangle + \langle \tau_{13}\tilde{S}_{13} \rangle + \langle \tau_{23}\tilde{S}_{23} \rangle\right). \tag{6.4}$$

Owing to isotropy before straining and to axisymmetry during straining, one can assume that $\langle \tau_{13}\tilde{S}_{13} \rangle = \langle \tau_{12}\tilde{S}_{12} \rangle$, $\langle \tau_{33}\tilde{S}_{33} \rangle = \langle \tau_{22}\tilde{S}_{22} \rangle$. During straining, the $\langle \tau_{23}\tilde{S}_{23} \rangle$ term is not available even assuming axisymmetry. Therefore, this term is not included and the dissipation is approximated by

$$\langle \tau_{ij}\tilde{S}_{ij} \rangle \approx \langle \tau_{11}\tilde{S}_{11} \rangle + 2\langle \tau_{22}\tilde{S}_{22} \rangle + 4\langle \tau_{12}\tilde{S}_{12} \rangle. \tag{6.5}$$

For isotropic turbulence before straining, it can be proven that the 23-term contributes 20% of the total amount of dissipation. During straining, the 11- and 22-components are significantly larger than other terms. Therefore, the error introduced by not including the 23-term is 20% initially, and below 20% during straining. A similar approximation is made for the rate-of-strain magnitude:

$$|\tilde{S}| \approx \left(2\tilde{S}_{11}^2 + 4\tilde{S}_{22}^2 + 8\tilde{S}_{12}^2\right)^{1/2}. \tag{6.6}$$

All the subsequent analysis is based on the approximation of discarding the 23-component.

6.3. *Evolution of subgrid energy dissipation*

The SGS dissipation $\Pi(t)$ is evaluated by taking averages over the 10 instantaneous distributions available for each time step. $\Pi(t)$ is a third-order moment, which requires many samples to achieve statistical convergence, and ten two-dimensional data sets at each time is insufficient for full convergence. However, the main trends can already be identified in figure 16(*a*), which shows $\Pi(t)$ at different scales as a function of time. As in previous figures, the extremes of the vertical bars represent averages over subsets of the data (first six and last six sets). During the initial stage of isotropic turbulence, the SGS dissipation is smaller than the dissipation rate ϵ_0 estimated from the energy spectrum in § 3 (the difference is partially a result of neglecting the 23-term, but may also be due to two-dimensional filtering). A similar discrepancy was observed in the jet measurements of Liu *et al.* (1994).

As the plates are accelerated, the SGS dissipation increases rapidly because of the

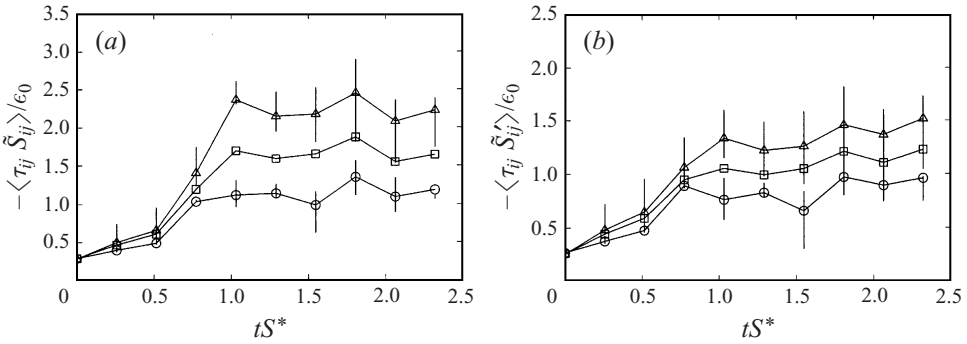

FIGURE 16. (*a*) Time evolution of total SGS energy dissipation from resolved to subgrid scales for different filter sizes. As in figure 15, vertical bars indicate (for $\Delta/\eta = 20$ and 40) partial averages from the first and last six vector maps. (*b*) Time evolution of net dissipation $\Pi^*(t)$. Circles: $\Delta/\eta = 20$, squares: $\Delta/\eta = 30$, triangles: $\Delta/\eta = 40$.

increase of the applied strain rate, and the response of turbulence to it. Figure 16(*a*) shows that at the initial stage, $\Pi(t)$ is independent of filter size, as expected for the SGS dissipation in the inertial range (while the SGS stress scales as $\Delta^{2/3}$, the resolved rate of strain scales as $\Delta^{-2/3}$). After the straining starts, the SGS stress is larger than the 2/3 power of scale (see figure 10), while the rate of strain is less dependent on scale because of the strong and uniform straining. Thus, $\Pi(t)$ increases with Δ. Figure 16(*b*) shows the net dissipation $\Pi^*(t)$, which also increases with applied straining and scale, but less than $\Pi(t)$ since the mean is not included in the strain rate.

Next, we compare the spatial distribution of the measured total (local) SGS energy dissipation $-\tau_{ij}\tilde{S}_{ij}$ with that predicted by the Smagorinsky and similarity models. The local and modelled SGS dissipation are evaluated using (6.5) and (6.6), but without spatial or ensemble averaging. Note that without averaging, the assumptions of isotropy and axisymmetry do not hold. However, we work under the assumption that qualitative features are not significantly affected. To evaluate the modelled SGS dissipation, one must fix the model coefficients c_s and c_L. For now, we use the values found in Liu *et al.* (1995), namely $c_s = 0.1$ and $c_L = 1$. As will be shown later, these coefficients depend on the straining. Figures 17 and 18 show the contour plots of the real and modelled SGS dissipation before and during straining (at $tS^* = 1.82$). In both cases, the similarity model reproduces coarse features of the distribution of real SGS dissipation. Energy backscatter is predicted in approximately the correct regions, although some discrepancies are evident. The Smagorinsky model predicts some of the positive regions of $-\tau_{ij}\tilde{S}_{ij}$ about as well as the similarity model. However, by construction, it does not reproduce any backscatter.

6.4. *Model coefficients by SGS dissipation balance*

6.4.1. *Similarity model*

From the condition that a model provides the correct rate of SGS energy dissipation, the coefficient in the similarity model can be evaluated according to

$$c_L = \frac{\langle \tau_{ij}\tilde{S}_{ij}\rangle}{\langle L_{ij}\tilde{S}_{ij}\rangle}, \tag{6.7}$$

where L_{ij} is the resolved stress tensor as defined in (1.4). As seen in figure 19(*a*) before straining starts, $c_L \approx 1$, in agreement with previous findings (Liu *et al.* 1995).

https://doi.org/10.1017/S0022112099004504 Published online by Cambridge University Press

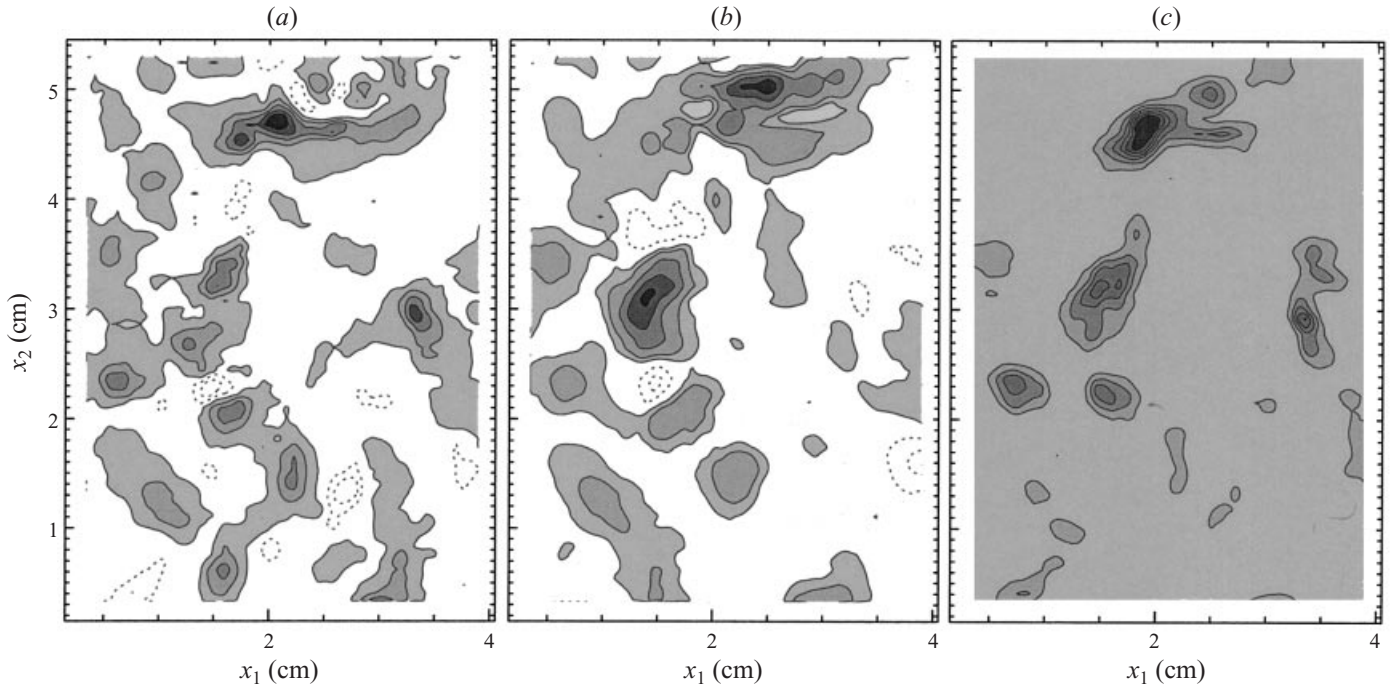

FIGURE 17. Contour plots of SGS dissipation fields from one data set before straining, at $tS^* = 0$. Filter size is $\Delta/\eta = 40$. (*a*) Real SGS dissipation. (*b*) Prediction of the similarity model. (*c*) Prediction of the Smagorinsky model. Darkest contour level: $0.025\,\mathrm{m^2\,s^{-3}}$, increment between lines: $-0.005\,\mathrm{m^2\,s^{-3}}$. The white regions are negative, corresponding to backscatter.

https://doi.org/10.1017/S0022112099004504 Published online by Cambridge University Press

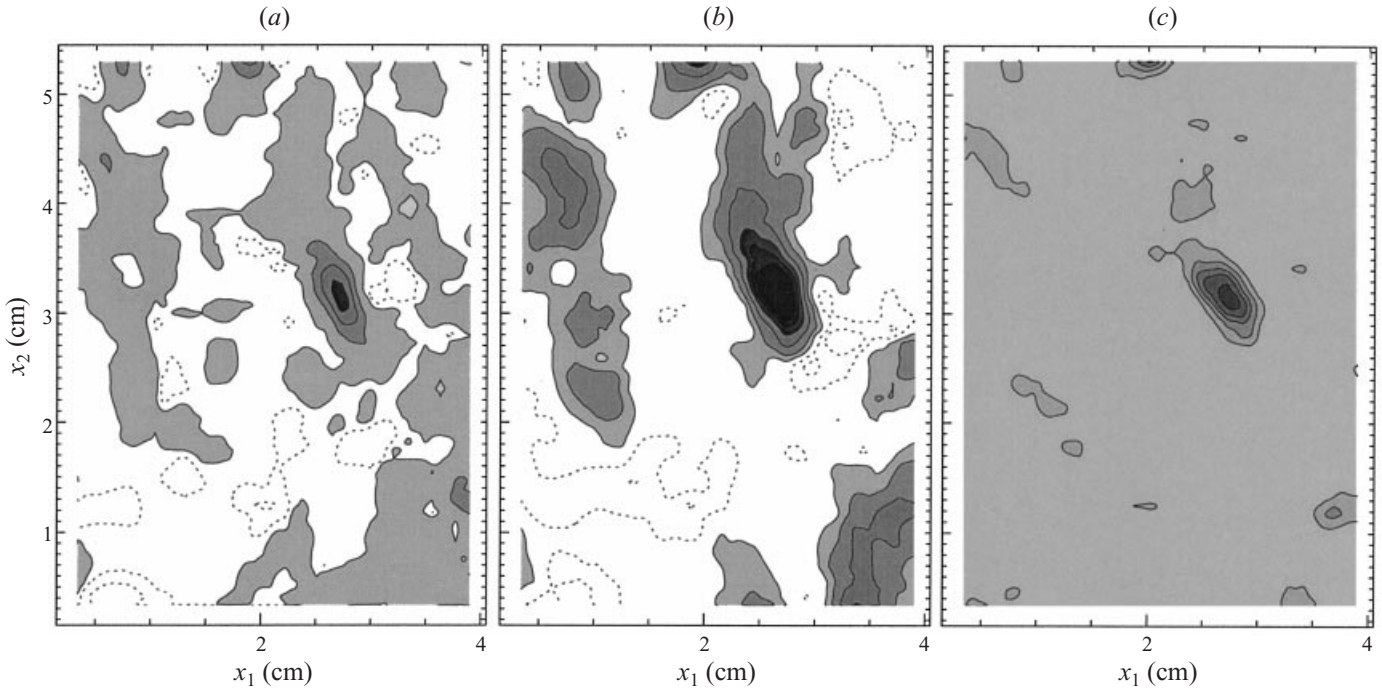

FIGURE 18. As figure 17 but at $tS^* = 1.82$. Darkest contour level: 0.15 $m^2\,s^{-3}$, increment between lines: $-0.03\,m^2\,s^{-3}$.

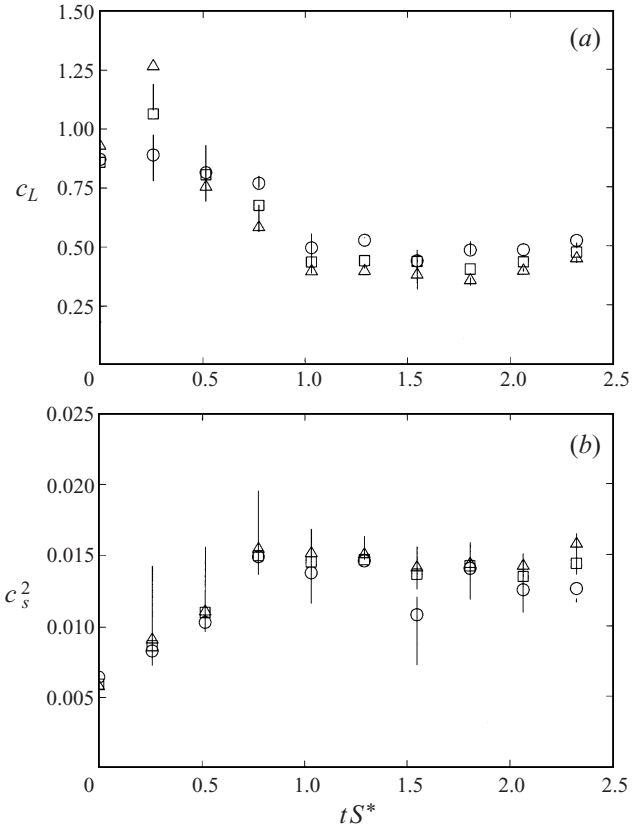

FIGURE 19. (*a*) Similarity model coefficient and (*b*) Smagorinsky model coefficient deduced from total SGS dissipation balance, at $\Delta/\eta = 20$ (circles), $\Delta/\eta = 30$ (squares) and $\Delta/\eta = 40$ (triangles). Vertical bars: same as in figure 16.

After the straining starts, c_L decreases rapidly and maintains a constant value of approximately $c_L \approx 0.45$ during the constant straining stage. Thus, according to this *a priori* test, the model with $c_L = 1$ would over-predict SGS dissipation. It is possible that this trend is caused by the increasing importance of mean and cross-stresses with increasing Δ, which would raise L_{ij} more than τ_{ij}. The observed strain dependence of the coefficient presents a basic problem for simulations in which fixed coefficients are used. Also, note that during straining c_L decreases with increasing Δ. Such scale-dependence of the coefficient poses difficulties for the dynamic model, which assumes scale-invariance (Meneveau & Lund 1997, see Porté-Agel, Meneveau & Parlange 1998 for a scale-dependent dynamic model).

If one requires the model to match the net dissipation Π^*, the coefficient should be evaluated according to

$$c_L^* = \frac{\langle \tau_{ij} \tilde{S}_{ij}^{(T)} \rangle}{\langle L_{ij} \tilde{S}_{ij}^{(T)} \rangle}. \tag{6.8}$$

The results (not shown) display trends similar to c_L, only that c_L^* decreases to about 0.6, instead of 0.45.

6.4.2. *Smagorinsky model*

For the Smagorinsky model the coefficient may be evaluated according to

$$c_s^2 = \frac{-\langle \tau_{ij}\tilde{S}_{ij}\rangle}{2\Delta^2 \langle |\tilde{S}|\tilde{S}_{ij}\tilde{S}_{ij}\rangle}, \tag{6.9}$$

where the mean total SGS dissipation is averaged in space and over all realizations at a given time. As shown in figure 19(*b*), before the straining starts the model coefficient, which varies between 0.06 to 0.14 (with a representative value $c_s \sim 0.09$), is close to the result of Liu *et al.* (1995). However it is lower than the standard value for isotropic turbulence ($c_s \sim 0.16$) possibly due to the effects of two-dimensional, instead of three-dimensional, filtering (Scotti, Meneveau & Lilly, 1993). During the acceleration phase the Smagorinsky coefficient increases, and then varies very little during the constant straining stage. Similar results (not shown) are obtained from a balance of net dissipation. The increase in coefficient implies that if one uses a constant model coefficient appropriate for isotropic turbulence, the Smagorinsky model would underpredict the dissipation. This trend contradicts the common expectation that the Smagorinsky model should over-dissipate in highly strained flows (see McMillan & Ferziger 1980; Smith & Yakhot 1993). To explain this contradiction, we examine the contributions of the turbulent, cross- and the applied straining parts of the SGS stress separately. These contributions are evaluated according to

$$c_{s-T}^2 = \frac{-\langle \tau_{ij}^{(T)}\tilde{S}_{ij}\rangle}{2\Delta^2\langle |\tilde{S}|\tilde{S}_{ij}\tilde{S}_{ij}\rangle}, \quad c_{s-C}^2 = \frac{-\langle \tau_{ij}^{(C)}\tilde{S}_{ij}\rangle}{2\Delta^2\langle |\tilde{S}|\tilde{S}_{ij}\tilde{S}_{ij}\rangle}, \quad c_{s-M}^2 = \frac{-\langle \tau_{ij}^{(M)}\tilde{S}_{ij}\rangle}{2\Delta^2\langle |\tilde{S}|\tilde{S}_{ij}\tilde{S}_{ij}\rangle}, \tag{6.10}$$

where

$$c_s^2 = c_{s-T}^2 + c_{s-C}^2 + c_{s-M}^2. \tag{6.11}$$

As shown in figure 20, these three coefficients have opposing trends. For the turbulent part, c_{s-T}^2 drops during straining, in agreement with McMillan & Ferziger (1980) who also computed the SGS stress solely in terms of the velocity fluctuations. Conversely, the dissipation associated with the cross-term increases substantially, and does not appear to depend on Δ. The applied straining part increases during the acceleration phase, and slightly decreases during the constant straining stage. The latter trend occurs since $\langle |\tilde{S}|\tilde{S}_{ij}\tilde{S}_{ij}\rangle$ increases due to the increasing turbulence during straining (figure 11 and RDT). Furthermore, c_{s-M}^2 increases with scale and at small Δ, c_{s-M}^2 is significantly smaller than the other terms.

The direct effect of the mean velocity gradient on the SGS stress arises because we are filtering in directions of mean velocity gradient, which gives rise to the cross- and mean terms. Obviously, these contributions would be absent if one filters only in directions in which the mean velocity is homogeneous, such as planes parallel to the wall in channel flow. In such a case, trends as in figure 21(*a*) should be expected. However, in typical simulations the entire c_s^2 is used, and the effects of cross- and mean terms are important.

6.5. *Mixed model*

We have seen in §6.4 that if one uses constant isotropic turbulence coefficients during rapid straining, the similarity model overpredicts the energy dissipation, while the Smagorinsky model underpredicts it. Thus, neither model can be regarded as universally valid for distorted turbulence. Their opposing trends motivate us to explore whether the mixed model (Bardina *et al.* 1980; Liu *et al.* 1994) can reproduce

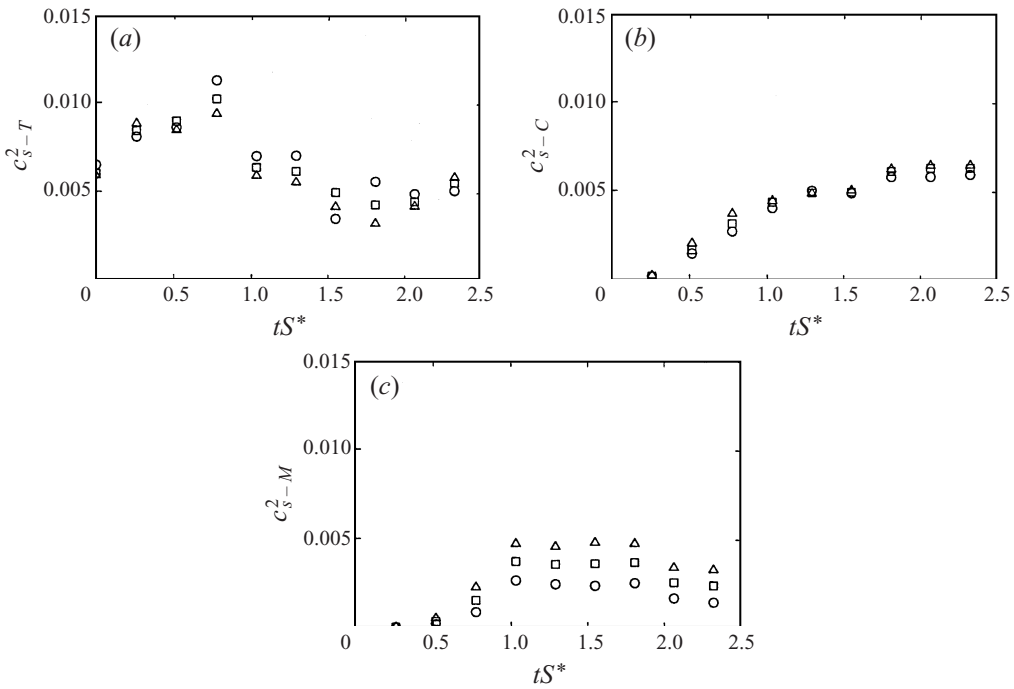

FIGURE 20. Contribution of the different terms to the Smagorinsky model coefficient: (*a*) turbulence term, (*b*) cross-term, (*c*) applied straining term. Symbols are the same as in figure 19.

the correct SGS energy dissipation with fixed coefficients, i.e. whether a mixed model is more universal than its constitutive parts. Let us write the mixed model as follows:

$$\mathscr{T}_{ij}^{\mathrm{mix}} = \alpha c_{Li} L_{ij} - 2(1-\alpha) c_{si}^2 \Delta^2 |\tilde{S}| \tilde{S}_{ij}, \tag{6.12}$$

where $c_{Li} = 1$ and $c_{si} = 0.09$ are the isotropic turbulence coefficients (see figure 19); α is a weight with value between 0 and 1 that is determined by matching with the data. Figures 21(*a*), 21(*b*) and 21(*c*) compare the real and modelled total SGS dissipation for $\alpha = 1$ (similarity), $\alpha = 0$ (Smagorinsky), and an adjusted value $\alpha = 0.3$ (mixed), respectively. As expected from figure 19, $\alpha = 1$ overpredicts and $\alpha = 0$ underpredicts the dissipation during straining. However, the fitted value $\alpha = 0.30$ does a remarkable job in predicting the correct total dissipation throughout the entire experiment, including the acceleration stage. We have repeated the analysis for the net dissipation, Π^*, and compared results with the mixed model using $\alpha = 0.35$. The conclusions are similar: at least in the present axisymmetric rapid straining, the mixed model with constant coefficients yields results that are significantly better than either the similarity or Smagorinsky models with fixed coefficients.

Figure 22(*a*) compares the dissipation by the turbulent stress $\Pi_T = -\langle \tau_{ij}^{(T)} \tilde{S}_{ij} \rangle$, with that of the cross- and mean stress, $\Pi_{C+M} = -\langle (\tau_{ij}^{(C)} + \tau_{ij}^{(M)}) \tilde{S}_{ij} \rangle$. Figure 22(*b*) compares the modeled dissipation produced by the similarity and Smagorinsky terms of the mixed model with $\alpha = 0.30$. Prior to straining, both the similarity and Smagorinsky terms contribute to the total dissipation, but during straining each term seems to assume a different role. The similarity term increases in a fashion which resembles the increase of Π_{C+M}, while the change in the Smagorinsky term is similar to the dissipation by the turbulent stress. The fact that Π_{C+M} evolves in a similar fashion to

https://doi.org/10.1017/S0022112099004504 Published online by Cambridge University Press

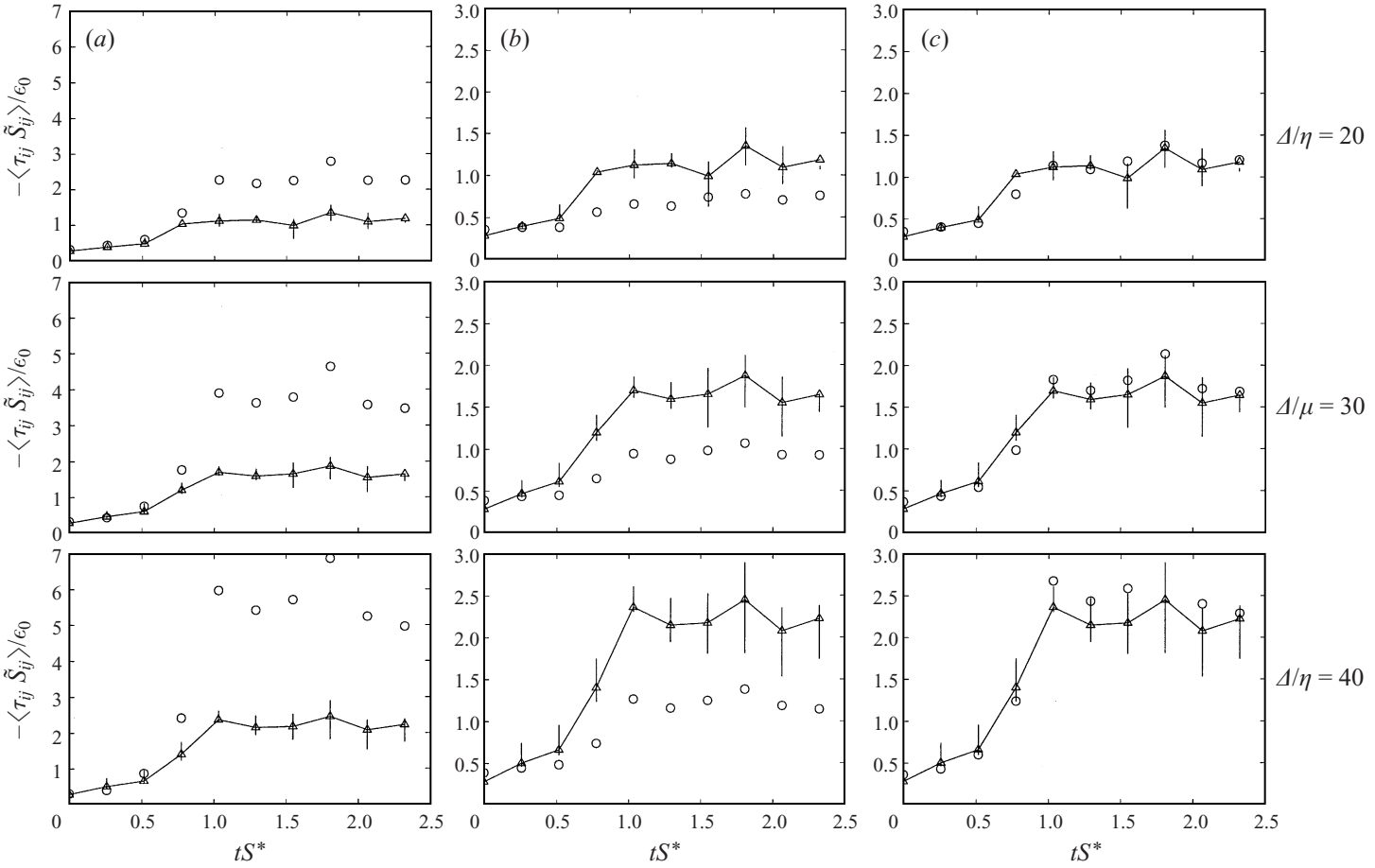

FIGURE 21. Real (triangles and solid line) and modeled (circles) total energy dissipation, using (*a*) the similarity model (mixed model with $\alpha = 1$ and a constant similarity coefficient), (*b*) the Smagorinsky (mixed model with $\alpha = 0$ and a constant Smagorinsky coefficient), (*c*) the mixed model with $\alpha = 0.3$.

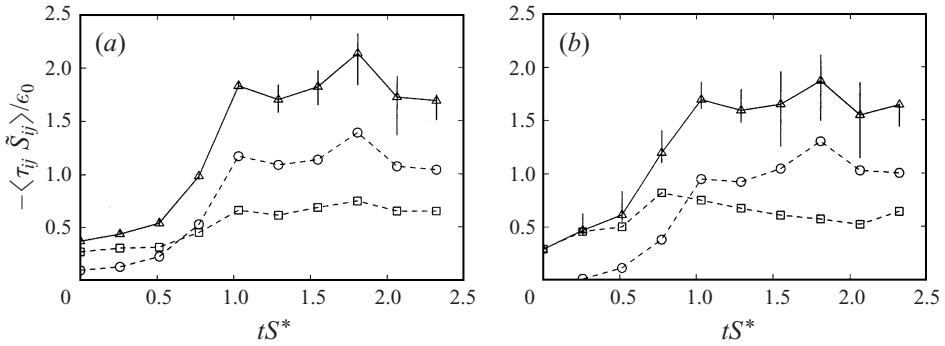

FIGURE 22. (*a*) Contributions of dissipation due to turbulent stress, $\Pi_T(t)$ (squares), and due to combined cross- and mean stresses, $\Pi_{C+M}(t)$ (circles), to the total real SGS dissipation (triangles). Δ/η=30. Vertical bars indicate partial averages from the first and last six vector maps. (*b*) Contributions to the modelled SGS dissipation from the similarity term, $\Pi_L(t) = -\alpha\ c_{Li}\ \langle L_{ij}\tilde{S}_{ij}\rangle$ (circles) and Smagorinsky term $\Pi_S(t) = (1-\alpha)\ c_{Si}^2\ 2\Delta^2\ \langle|\tilde{S}|\tilde{S}_{ij}\tilde{S}_{ij}\rangle$ (squares) in a mixed model with $\alpha = 0.3$. Triangles: total modelled dissipation Δ/η=30.

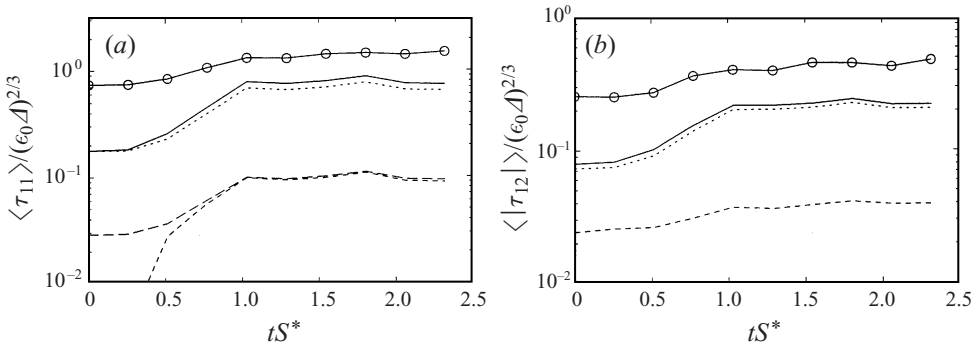

FIGURE 23. Real and modelled mean SGS stress, for $\alpha = 0.3$. Circles and solid line: real stress. Solid line: modelled stress using the mixed model with $\alpha = 0.3$. Dotted line: contribution from the similarity model. Short-dashed line: contribution from the Smagorinsky model. (*a*) Evolution of $\langle\tau_{11}\rangle$. Long dashed line is the average of the absolute value. (*b*) Evolution of $\langle|\tau_{12}|\rangle$.

$-\langle L_{ij}\tilde{S}_{ij}\rangle$ is not too surprising if one considers that L_{ij} may by itself be decomposed into contributions from mean, cross- and turbulent stresses. The mean and cross-stresses contain the mean flow in a similar fashion to the corresponding terms in the SGS stress, possibly accounting for some of the similar behaviour of the dissipation. In fact, it has often been argued (Zang *et al.* 1993; Salvetti & Banerjee 1995; Kang *et al.* 1998) that the role of the similarity term is to model the cross-stresses that arise in the Leonard decomposition of the SGS stress (Leonard 1974), while the eddy-viscosity term's role is to model the purely small-scale contributions. Presently observed trends are consistent with this view, even though there are differences between the present and Leonard's (1974) definition of cross-stresses. The latter involve the difference between full and filtered velocities, as opposed to the present definition involving the difference between full and mean velocities.

While reproducing the correct mean SGS dissipation is a very important requirement for a model, one may also be interested in determining how well the models reproduce the mean value, $\langle\tau_{ij}\rangle$, and the mean magnitude, $\langle|\tau_{ij}|\rangle$, of the stress. For the present data in homogeneous turbulence, the mean stress is spatially uniform

and therefore does not affect the mean flow. Its study is nevertheless of interest, to determine how much of the real SGS physics is captured by the models since in applications to non-homogeneous flows the stress divergence contributes to the mean resolved momentum flux. The mean values of the different contributors to the modelled τ_{11} are compared with the real mean value in figure 23(*a*). As can be seen, the modelled stress is dominated by the similarity term, which is significantly larger than the Smagorinsky term throughout the straining process. Since the mean of the Smagorinsky model is zero for unstrained, isotropic turbulence, we also plot the average of its absolute value. The results, also shown in figure 23(*a*), illustrate that the mean magnitude of this term is low as well. This fact preserves the high correlation (and smaller square error) of the similarity term with the real stress also for the mixed model during the entire straining process. However, the modelled mean value of the total SGS stress is considerably lower than the real value. Figure 23(*b*) shows similar trends for the mean absolute values of the off-diagonal, 12-component of the SGS stress. As a result, an α-value that models the correct dissipation leads to an underprediction of the mean stress and its mean magnitude. A value $\alpha = 1$ would yield the correct stress magnitude and dissipation for isotropic, unstrained turbulence (Liu *et al.* 1995; Cook 1997), but would overpredict the dissipation and its trends during the rapid straining. The fact that a single similarity model coefficient is unable to simultaneously reproduce the magnitude of stress and SGS dissipation during rapid straining demonstrates that there still exists significant room for improvement of the similarity and mixed models.

Finally, the value of α found here for both axisymmetric straining and isotropic turbulence may not be generally valid for other flows. The dynamic procedure applied to the mixed model (Liu *et al.* 1995; Vreman *et al.* 1994; Salvetti & Banerjee 1995; Ansari *et al.* 1998) has the potential of determining the appropriate coefficients. We have attempted to study the dynamic model based on the present data. However, owing to the large spatial extent of the test filter (4Δ for the dynamic similarity and mixed models), treatment of end-effects has forced us to eliminate large amounts of data along the border of the vector maps (about 80% for $\Delta = 30\eta$). The concomitant rise in uncertainty due to poor statistical convergence rendered the results inconclusive. A study of dynamic versions of the models considered here must therefore await larger data sets.

7. Summary and conclusions

7.1. *Experimental apparatus to generate isotropic turbulence and rapid straining:*

A special test facility for studying the response of isotropic turbulence to rapid straining has been constructed. Its design decouples the strain rate and the mechanism for generating turbulence, and as a result provides the capability for generating the desired high levels of turbulence and rapid straining independently. The turbulence is generated by four spinning grids located symmetrically around the sample area. Cinematic PIV is used for measuring the velocity distribution. Performance tests lead to the following conclusions:

(*a*) There is very little mean flow in the sample area, which allows one to follow the evolution of the same flow structure over relatively long periods of time.

(*b*) The turbulence spectra in all three directions are similar, all having a $-\frac{5}{3}$ slope over a substantial fraction of the spectrum.

(*c*) The turbulence is reasonably homogeneous in space over the sample area,

although more data sets will be required to obtain better-converged statistics at every point to better ensure homogeneity.

(*d*) A relatively elevated Reynolds number ($R_\lambda \sim 290$) is achieved, without the need for high flow rates.

Axisymmetric rapid straining is produced by pushing two disks towards each other, creating a stagnation point flow. The time-dependent velocity of the disks is set so as to produce a nearly steady and uniform strain rate in the flow, after an acceleration period.

(*a*) The tests confirm that the induced mean velocity field conforms to these requirements.

(*b*) The non-dimensional straining achieved is $S^*k_0/\epsilon_0 \sim 17$.

Thus, the tests show that the desired flow conditions are achieved in this experimental facility.

7.2. *Evolution of subgrid scales during straining:*

A priori tests of subgrid motions and SGS stresses in the rapidly strained turbulence lead to the following conclusions:

(*a*) During rapid straining, the measured normalized SGS stresses (their turbulent part) are significantly more isotropic than the prediction of RDT. The isotropy increases as the filter scale decreases. While small scales remain more isotropic, they become proportionally more energetic than the large scales.

(*b*) Differences between subgrid and Reynolds stresses could not be explored in detail owing to a lack of statistical convergence.

(*c*) Scale similarity persists during rapid straining. Consequently, the similarity model improves upon the Smagorinksy model as quantified by both the correlation coefficient between real and modeled stress elements, and by the square-error between the real and modelled SGS force (a two-dimensional approximation).

(*d*) The distortion has a strong effect on the SGS dissipation at all filter sizes considered. This result is consistent with the very strong, direct effect of sudden, large-scale forcing on inertial-range energy transfer observed in DNS of initially isotropic turbulence (Yeung & Brasseur 1991).

(*e*) Large-scale rapid straining introduces three types of stresses, identified in this paper as turbulent stress, cross-stress, and mean-straining stress. Each displays different trends with scale. As a result, their relative impact on the SGS energy dissipation, $\Pi(t)$, model coefficients, etc., depends on scale.

(*f*) During the distortion, $\Pi(t)$ is found to strongly increase with scale. More energy is fed to the large scales than to the small scales, setting up a strong non-equilibrium in the cascade process. Similar conclusions are reached based on the 'net' dissipation Π^*, which takes into account the cancellation that arises from the divergence term in the resolved kinetic energy equation.

(*g*) Model coefficients determined from dissipation in undistorted isotropic turbulence are inappropriate during rapid straining. The similarity model with fixed coefficient overpredicts, and the Smagorinsky model underpredicts the SGS dissipation. The latter surprising effect occurs because when the mean velocity is included in the definition of τ_{ij}, and one is filtering in the direction of mean velocity gradient, the cross- and mean-straining terms contribute substantially to the real dissipation. Since in LES the mean velocity field is usually unknown *a priori*, one seeks to model the entire SGS stress, including the cross- and mean-straining terms.

(*h*) A mixed model that cancels the opposing trends of the similarity and Smagorinsky models does remarkably well in determining the dissipation during the entire

straining process, at all filter scales considered. Note that these (*a priori*) observations are based on the real data and not on what may occur (*a posteriori*) in LES. In simulations, the model may respond differently since it is then based on possibly unrealistic data of the numerically simulated resolved field.

(*i*) In terms of the SGS stress, the Smagorinsky term is much smaller than the similarity term throughout the distortion. Consequently the correlation coefficient of the mixed model with the real stress remains essentially as large as that of the similarity model. Nevertheless, the modelling of the mean value of the SGS stress is surprisingly poor during the distortion. The mixed (or similarity) model optimized for accurate prediction of SGS dissipation severely underpredicts $\langle \tau_{ij} \rangle$ during the distortion. For $\langle \tau_{11} \rangle$, there is a discrepancy of nearly a factor of 3. Further improvements in the modelling are clearly needed.

The present results are obtained by separating large from small scales using a physical-space box filter. Some sensitivity of the present results to the type of filtering cannot be ruled out. Moreover, the conclusions reached in this work are derived from turbulence undergoing rapid axisymmetric expansion at a single strain rate. Further studies should be undertaken to consider other strain-rate magnitudes, and other types of distortions such as axisymmetric contraction, plane strain, rapid rotation, and the return to isotropy once the distortion has ended. Non-equilibrium effects in non-homogeneous flows are also of interest. Recently, Piomelli, Coleman & Kim (1997) examined the Smagorinsky and similarity models in channel flow undergoing two types of perturbations: rapid streamwise acceleration, and sudden lateral motion of the wall. Consistent with our present findings, the mixed model was found to realistically reproduce the SGS dissipation. An interesting difference is that in their study the filtering is done in planes parallel to the wall where the flow is spatially homogeneous even in the mean. Thus, as opposed to our case, there is no direct contribution from the mean shearing to the SGS stress. Our results show that even in cases where there is such a direct contribution (and we show that it can be large for rapid distortion) the mixed model performs well in predicting the SGS dissipation, but not the mean stress.

We would like to thank Professor O. Knio for interesting discussions and comments on this work. Thanks are due also to Professor G. Chirikjian, for his idea of using cams to actuate the disks in the experiment, and to Professor W. C. Reynolds for making us aware of Choi's (1983) experimental results on slow axisymmetric expansion. Technical assistance with the electronics by S. King and with the optics by L. Bertuccioli and S. Gopalan are also acknowledged. This research is sponsored by the Office of Naval Research, under grant N00014-92-J-1109, monitored by Dr P. Purtell. Computations were supported in part by an NSF equipment grant (CTS-9506077).

REFERENCES

Adrian, R. J. 1990 Stochastic estimation of subgrid scale motions. *Appl. Mech. Rev.* **43**, 214.

Ansari, A., Mangiavacchi, N., Kang, S. & Akhavan, R. 1998 On subgrid-scale modelling of turbulence: Part 1. analysis of subgrid interactions in a numerically simulated turbulent jet. (Submitted.)

Bardina, J. 1983 Improved turbulence models based on large eddy simulation of homogeneous, incompressible, turbulent flows. PhD thesis, *Rep.* TF-19: Mechanical Engineering, Stanford University.

Bardina, J., Ferziger, J. H. & Reynolds, W. C. 1980 Improved subgrid scale models for large eddy simulation. *AIAA Paper* 80-1357.

Batchelor, G. K. & Proudman, I. 1954 The effects of rapid distortion of a fluid in turbulent motion. *Q. J. Mech. Appl. Maths* **7**, 83.

Bertuccioli, L., Gopalan, S. & Katz, J. 1996 Image shifting for PIV using birefringent and ferroelectric liquid crystals. *Exps. Fluids* **21**, 341–346.

Borue, V. & Orszag, S. 1998 Local energy flux and subgrid-scale statistics in three-dimensional turbulence. *J. Fluid Mech.* **366**, 1–31.

Champagne, F. H., Harris, V. G. & Corrsin, S. 1979 Experiments on nearly homogeneous turbulent shear flow. *J. Fluid Mech.* **41**, 81.

Choi, K. S. 1983 A study of the return to isotropy of homogeneous turbulence. PhD thesis, Cornell University.

Chollet, J. & Lesieur, M. 1981 Parametrization of small scales of three-dimensional isotropic turbulence utilizing spectral closures. *J. Atmos. Sci.* **38**, 2747.

Clark, R. A., Ferziger, J. H. & Reynolds, W. C. 1979 Evaluation of subgrid models using an accurately simulated turbulent flow. *J. Fluid Mech.* **91**, 1.

Cook, A. 1997 Determination of the constant coefficient in scale similarity models of turbulence. *Phys. Fluids* **9**, 1485–1487.

Cook, A. & Riley, J. J. 1994 A subgrid model for equilibrium chemistry in turbulent flows. *Phys. Fluids* **6**, 2868–2870.

Crow, S. C. 1968 Viscoelastic properties of fine-grained incompressible turbulence. *J. Fluid Mech.* **33**, 1.

Deardorff, J. W. 1970 A numerical study of three-dimensional turbulent channel flow at large Reynolds numbers. *J. Fluid Mech.* **41**, 453.

Devenport, W. J. & Simpson, R. L. 1990 Time-dependent and time-averaged turbulence structure near the nose of a wing-body junction. *J. Fluid Mech.* **210**, 23.

Dong, R., Chu, S. & Katz, J. 1992 Quantitative visualization of the flow structure within the volute of a centrifugal pump, part a: Technique. *Trans. ASME J. Fluids Engng* **114**, 390–395.

Farge, M. & Rabreau, G. 1988 Wavelet transform to detect and analyze coherent structures in two-dimensional turbulent flows. *C. R. Acad. Sci. Paris* II **307**, 1479.

Ganapathy, S. & Katz, J. 1995 Drag and lift forces on a bubble entrained by a vortex. *Phys. Fluids* **7**, 389.

Gence, J. N. & Mathieu, J. 1979 On the application of successive plane strains to grid-generated turbulence. *J. Fluid Mech.* **93**, 501.

Germano, M., Piomelli, U., Moin, P. & Cabot, W. H. 1991 A dynamic subgrid-scale eddy viscosity model. *Phys. Fluids* A **3**, 1760.

Hopfinger, E. J. & Toly, J. A. 1976 Spatially decaying turbulence and its relation to mixing across density interfaces. *J. Fluid Mech.* **78**, 155–175.

Horiuti, K. 1997 A new dynamic two-parameter mixed model for large-eddy simulation. *Phys. Fluids* **9**, 3443–3464.

Hunt, J. C. R. & Carruthers, D. J. 1990 Rapid distortion theory and the 'problems' of turbulence. *J. Fluid Mech.* **212**, 497.

Hunt, J. C. R., Wray, A. A. & Moin, P. 1988 Eddies, streams, and convergence zones in turbulent flows. In *Proc. Summer Program 1988 Stanford University*, vol. II, p. 193.

Kang, S., Ansari, A. & Akhavan, R. 1998 On subgrid-scale modelling of turbulence: Part 2. A dynamic two-component model for large-eddy simulation of turbulent flows. (Submitted.)

Kassinos, S. C. 1994 A structure-based model for the rapid distortion of homogeneous turbulence. PhD thesis TF-61, Stanford University.

Kevlahan, N. K.-R. & Hunt, J. C. R. 1997 Nonlinear interactions in turbulence with strong irrotational straining. *J. Fluid Mech.* **337**, 333.

Kida, S. & Hunt, J. C. R. 1989 Interaction between different scales of turbulence over short times. *J. Fluid Mech.* **201**, 411.

Kraichnan, R. H. 1976 Eddy viscosity in two and three dimensions. *J. Atmos. Sci.* **33**, 1521.

Lee, M. J. 1985 Numerical experiments on the structure of homogeneous turbulence. PhD thesis TF-24, Stanford University.

Lee, M. J. 1989 Distortion of homogeneous turbulence by axisymmetric strain and dilation. *Phys. Fluids* A **1**, 1541–1557.

Leonard, A. 1974 Energy cascade in large-eddy simulations of turbulent fluid flows. *Adv. Geophys.* **18**, 237.

Lesieur, M. & Métais, O. 1996 New trends in large-eddy simulations of turbulence. *Ann. Rev. Fluid Mech.* **28**, 45.

Lilly, D. K. 1992 A proposed modification of the Germano subgrid scale closure method. *Phys. Fluids* A **4**, 633.

Liu, S., Meneveau, C. & Katz, J. 1994 On the properties of similarity subgrid-scale models as deduced from measurements in a turbulent jet. *J. Fluid Mech.* **275**, 83.

Liu, S., Meneveau, C. & Katz, J. 1995 Experimental study of similarity subgrid-scale models of turbulence in the far-field of a jet. *Appl. Sci. Res.* **54**, 177.

McMillan, O. J. & Ferziger, J. H. 1979 Direct testing of subgrid-scale models. *AIAA J.* **17**, 1340.

Meneveau, C. 1994 Statistics of turbulence subgrid-scale stresses: Necessary conditions and experimental tests. *Phys. Fluids* A **6**, 815.

Meneveau, C. & Lund, T. S. 1997 Dynamic model and scale-dependent coefficients in the viscous range of turbulence. *Phys. Fluids* **9**, 3932.

Meneveau, C., Lund, T. & Cabot, W. H. 1996 A lagrangian dynamic subgrid-scale model of turbulence. *J. Fluid Mech.* **319**, 353–385.

Meneveau, C., Lund, T. & Moin, P. 1992 Search for subgrid scale parameterization by projection pursuit regression. *Proc. CTR Summer Program., Stanford Univ.* vol IV, pp. 61–81.

Monin, A. & Yaglom, A. 1971 *Statistical Fluid Mechanics.* MIT Press.

Moser, R. D. & Adrian, R. J. 1998 Turbulence data for LES development and validation. *Proc. FEDSM'98, 1998 ASME Fluids Engng Division Summer Meeting Paper* FEDSM98-5092 (on CD-ROM).

O'Neil, J. & Meneveau, C. 1997 Subgrid-scale stresses and their modeling in the turbulent plane wake. *J. Fluid Mech.* **349**, 253.

Piomelli, U., Cabot, W. H., Moin, P. & Lee, S. 1991 Sub-grid scale backscatter in turbulent and transitional flows. *Phys. Fluids* A **3**, 1766–1771.

Piomelli, U., Coleman, G. N. & Kim, J. 1997 On the effects of nonequilibrium on the subgrid-scale stresses. *Phys. Fluids* **9**, 2740–2748.

Piomelli, U., Yu, Y. & Adrian, R. 1996 Subgrid-scale energy transfer and near-wall turbulence structure. *Phys. Fluids* **8**, 215–224.

Piomelli, U. & Zang, T. A. 1991 Large-eddy-simulation of transitional channel flow. *Comput. Phys. Commun.* **65**, 224.

Porté-Agel, F., Meneveau, C. & Parlange, M. B. 1998 A scale-dependent dynamic model for large-eddy simulation: application to the atmospheric boundary layer. Preprint.

Rogallo, R. & Moin, P. 1984 Numerical simulation of turbulent flows. *Ann. Rev. Fluid. Mech.* **16**, 99.

Roth, G., Hart, D. & Katz, J. 1995 Feasibility of using the l64720 video motion estimation processor (MEP) to increase efficiency of velocity map generation for PIV. *Proc. ASME/EALA Sixth Intl Symp. on Laser Anemometry*, FED vol. 229, pp. 387–396.

Saddoughi, S. G. 1993 Local isotropy in distorted turbulent boundary layers. In *Center for Turbulence Research, Annual Research Briefs, Stanford University*, p. 347.

Salvetti, M. V. & Banerjee, S. 1995 A-priori tests of a new dynamic subgrid-scale model for finite-difference large-eddy simulations. *Phys. Fluids* **7**, 2831–2847.

Savill, A. M. 1987 Recent developments in rapid distortion theory. *Ann. Rev. Fluid Mech.* **19**, 531.

Scotti, A., Meneveau, C. & Lilly, D. K. 1993 Generalized Smagorinsky model for anisotropic grids. *Phys. Fluids* A **5**, 2306.

Smagorinsky, J. 1963 General circulation experiments with the primitive equations. I. The basic experiment. *Mon. Weather Rev.* **91**, 99.

Smith, L. M. & Yakhot, V. 1993 Short- and long-time behavior of eddy-viscosity models. *Theor. Comput. Fluid Dyn.* **4**, 197.

Speziale, C. 1991 Analytical methods for the development of Reynolds-stress closures in turbulence. *Ann. Rev. Fluid Mech.* **23**, 107.

Srdic, A., Fernando, H. J. S. & Montenegro, L. 1996 Generation of nearly isotropic turbulence using two oscillating grids. *Exps. Fluids* **20**, 395–397.

Sreenivasan, K. R. 1985 The effect of contraction on a homogeneous turbulent shear flow. *J. Fluid Mech.* **54**, 187.

Tavoularis, S. & Corrsin, S. 1981 Experiments on nearly homogeneous turbulent shear flow with a uniform temperature gradient. Part 1. *J. Fluid Mech.* **104**, 311.

Tavoularis, S. & Karnik, U. 1989 Further experiments on the evolution of turbulent stresses and scales in uniformly sheared turbulence. *J. Fluid Mech.* **204**, 457.

Townsend, A. A. 1976 *Structure of Turbulent Shear Flow*. Cambridge University Press.

Tucker, H. J. & Reynolds, A. J. 1968 The distortion of turbulence by irrotational plane strain. *J. Fluid Mech.* **32**, 657.

Voke, P. R. 1996 Subgrid-scale modeling at low mesh Reynolds number. *Theor. Comp. Fluid Dyn.* **8**, 131–143.

Vreman, B., Geurts, B. & Kuerten, H. 1994 On the formulation of the dynamic mixed subgrid-scale model. *Phys. Fluids* **6**, 4057–4059.

Vreman, B., Geurts, B. & Kuerten, H. 1997 Large eddy simulation of the turbulent mixing layer. *J. Fluid Mech.* **339**, 357–390.

Wu, X. & Squires, K. 1997 Large eddy simulation of an equilibrium three-dimensional turbulent boundary layer. *AIAA J.* **35**, 67–74.

Yakhot, A., Orszag, S. A. & Yakhot, V. 1989 Renormalization group formulation of large-eddy simulations. *J. Sci. Comput.* **4**, 139.

Zang, Y., Street, R. L. & Koseff, J. 1993 A dynamic mixed subgrid-scale model and its application to turbulent recirculating flows. *Phys. Fluids* A **5**, 3186–3196.